

Order–Disorder in Fe–Si Alloys: Implications for Seismic Anisotropy and Thermal Evolution of Earth’s Inner Core

Cong Liu,^{1,*} Xin Deng,¹ and R. E. Cohen^{1,†}

¹*Extreme Materials Initiative, Earth and Planets Laboratory, Carnegie Institution for Science,
5241 Broad Branch Road NW, Washington, District of Columbia 20015, USA*

(Dated: December 1, 2025)

Understanding the structure and dynamics of Earth’s inner core is essential for constraining its composition, thermal evolution, and seismic properties. Silicon is a probable major component of Earth’s core. Using first-principles molecular dynamics and thermodynamic modeling, we investigate the structural, elastic, and transport properties of Fe–Si alloys at high pressures and temperatures. By computing the Gibbs free energies of B2, hcp, fcc, and bcc solid solutions, we construct the Fe–Si phase diagram applicable to the Earth’s inner core. Our results reveal a pronounced miscibility gap between hcp and B2 Fe–Si, with the two phases coexisting over the compositional range of 6–11 wt% Si at 6000 K. The B2 Fe–Si alloy exhibits strong single-crystal shear anisotropy (22.9% at 6000 K) compared to the nearly isotropic hcp phase (0.6%), and yields a shear wave velocity ($V_S = 3.73$ km/s) and Poisson’s ratio consistent with seismological observations. Moreover, the computed transport properties reveal substantially lower thermal conductivity of B2 Fe–Si relative to pure iron or hcp Fe–Si under inner-core conditions. These results imply that Earth’s inner core likely comprises multiple phases, whose distribution and crystallographic texture critically influence its seismic and thermal properties.

INTRODUCTION

Whether Earth’s solid inner core adopts the hexagonal close-packed (hcp) or body-centered cubic (bcc) structure of iron has remained a subject of long-standing debate [1–6]. Static and dynamic compression experiments show that pure Fe remains hcp structured through the Earth’s inner core pressures and temperatures. [4, 6]. Ab initio molecular-dynamics free-energy calculations show that although pure bcc Fe is entropically favored at core temperatures, it remains higher free energy than hcp Fe [7–12]. However, seismic observations reveal pronounced shear-wave anisotropy, with shear-wave velocities varying by up to 15–18% depending on propagation direction—significantly larger than predicted for hcp Fe and consistent with the lower shear modulus and intrinsic elastic anisotropy of bcc Fe [13–19]. Furthermore, hcp Fe is predicted to exhibit nearly isotropic sound velocities under inner-core conditions [20], in contrast to the strong anisotropy observed seismologically [21–24].

Seismological observations indicate that Earth’s core is less dense and has higher sound velocities than pure iron. Light elements such as H, C, O, Si, and S, incorporated during planetary accretion and differentiation [25, 26] are inferred to reside in both the liquid outer core, which contains up to 20 wt.% light elements, and the solid inner core (IC), with a much smaller fraction [26]. First-principles calculations and high-pressure experiments have long been employed to constrain the composition of Earth’s core [27, 28]. Among the potential light elements, silicon stands out as a particularly compelling candidate [29, 30]. Geochemical evidence also

suggests that silicon is concentrated in the core; Si isotope systematics in terrestrial and lunar basalts reveal a heavy $\delta^{30}\text{Si}$ signature consistent with early segregation of silicon into Earth’s metallic core [31]. Estimates of silicon content in the solid inner core vary, with recent studies suggesting approximately 4.1 wt.% Si [32], whereas others propose lower values around 2.3 wt.% [26]. These studies, however, generally assume that Si is incorporated into hcp Fe alloys within the inner core. High-pressure experiments on Fe–Si alloys [33–40] demonstrate that silicon stabilizes bcc or B2 phases near the melting curve, with bcc/B2 coexisting with hcp depending on composition [41]. The coexistence of these phases in the inner core allows higher Si concentrations, consistent with seismological constraints, as demonstrated below. Computational studies [42–44] highlight the entropy-driven competition among hcp, fcc, bcc, and B2 structures under the high temperatures of Earth’s core. Hybrid Monte Carlo simulations combined with deep-learning interatomic potentials [45] revealed a complex Fe–Si phase diagram at inner-core pressures (~ 330 GPa) and high temperatures, identifying a re-entrant bcc phase stabilized by pronounced Si short-range order (SRO) originating from B2-type configurations. This approach also shifts the phase boundary between the hcp phase and the hcp + B2 coexistence region toward higher Si contents compared with previous experiments [36], underscoring the stabilizing influence of configurational disorder under core conditions.

Whereas pure iron crystallizes in the hcp phase under inner-core conditions [6], the compound FeSi adopts the B2 (CsCl-type) structure [35]. For solid solutions of Fe with FeSi, the excess Fe partitions between Fe and Si sites within the B2 lattice. This represents a case of long-range convergent ordering [46–49]. If the Fe and Si atoms are fully disordered, the two sites become equiv-

* Corresponding author: cliu10@carnegiescience.edu

† rcohen@carnegiescience.edu

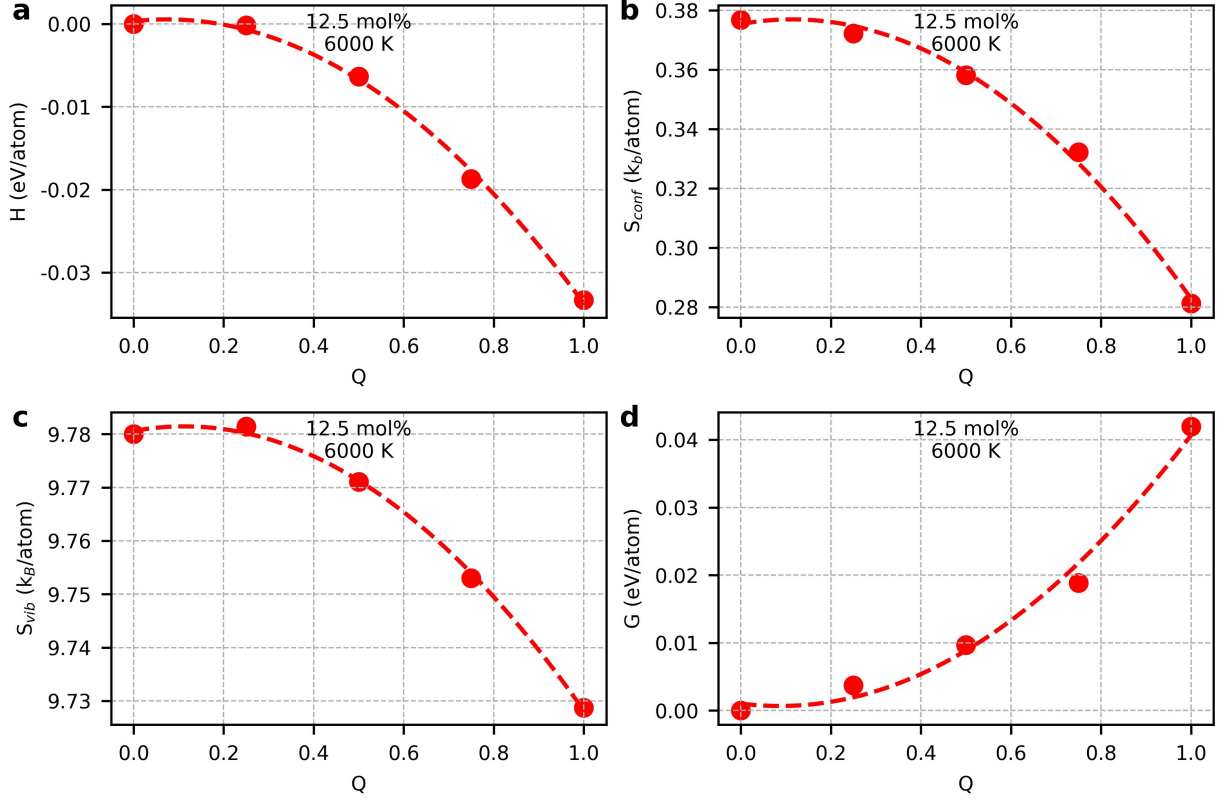


Fig. 1. **Effects of order parameter in B2 Fe–Si alloys.** Illustrated for a representative composition of $\text{Fe}_{0.875}\text{Si}_{0.125}$ (12.5 mol% Si), where $Q = 0$ and $Q = 1$ denote completely disordered (bcc) and fully ordered (B2) states, respectively. **a** Enthalpy at 330 GPa 6000 K, **b** configurational entropy, **c** vibrational entropy at 330 GPa and 6000 K, and **d** Gibbs free energy at 330 GPa and 6000 K as functions of order parameter Q . The enthalpies and Gibbs free energy at $Q=0$ have been shifted to zero for illustration.

alent, producing a bcc structure; partial ordering yields the B2 phase. Here we adopt a similar approach to that recently applied to high-pressure Mg_2GeO_4 , in which Mg and Ge disorder on different crystallographic sites, i.e., non-convergently [50–52].

Fe–Si alloys exhibit variable degrees of chemical order depending on P , T , and composition. Theoretical studies have considered both ideal and non-ideal [45] mixing at high P – T conditions. Here we combine density functional theory calculations, the special quasirandom structure (SQS) method [53, 54], and *ab initio* molecular dynamics and compute the Fe–Si binary phase diagram and quantify how order–disorder transitions influence thermal and electrical conductivity as well as seismic anisotropy of Fe–Si alloys under Earth’s inner-core conditions.

RESULTS

We constructed long-range ordered configurations of B2, hcp, and fcc structures for $\text{Fe}_{1-X}\text{Si}_X$ for mole fraction X from 0 to 0.5, varying the Si occupancy at each inequivalent lattice site (Fig. S1 in the Supplemental Ma-

terials). For hcp and fcc, we also allow partitioning of Si atoms across two inequivalent sites, breaking the hcp and fcc symmetry. Each Fe–Si composition and site concentration (Table S1 in the supplemental materials) were used to generate quasi-random configurations in a $4 \times 4 \times 4$ (128-atom) supercell with an order parameter Q ranging from 0 (fully disordered) to 1 (fully ordered) (see Methods). Enthalpies of these configurations were obtained from first-principles molecular dynamics (FPMD) simulations at selected temperatures, averaged over equilibrium segments of the trajectory. As shown in Fig. S2 in the Supplemental Materials, the enthalpy of the B2 phase decreases significantly with increasing Q , particularly at higher Si concentrations. At zero temperature, pure hcp Fe coexists with pure ordered FeSi.

The Gibbs free energy as a function of the order parameter (Q) can be expressed in terms of enthalpy, configurational entropy, and vibrational entropy:

$$G(P, T) = H(T, V) - (S_{\text{conf}} + S_{\text{vib}})T, \quad (1)$$

$$= E(T, V) + PV + ZPE - (S_{\text{conf}} + S_{\text{vib}})T, \quad (2)$$

where $E(T, V)$ is the total internal energy, including vibrational contributions; ZPE is the zero-point energy;

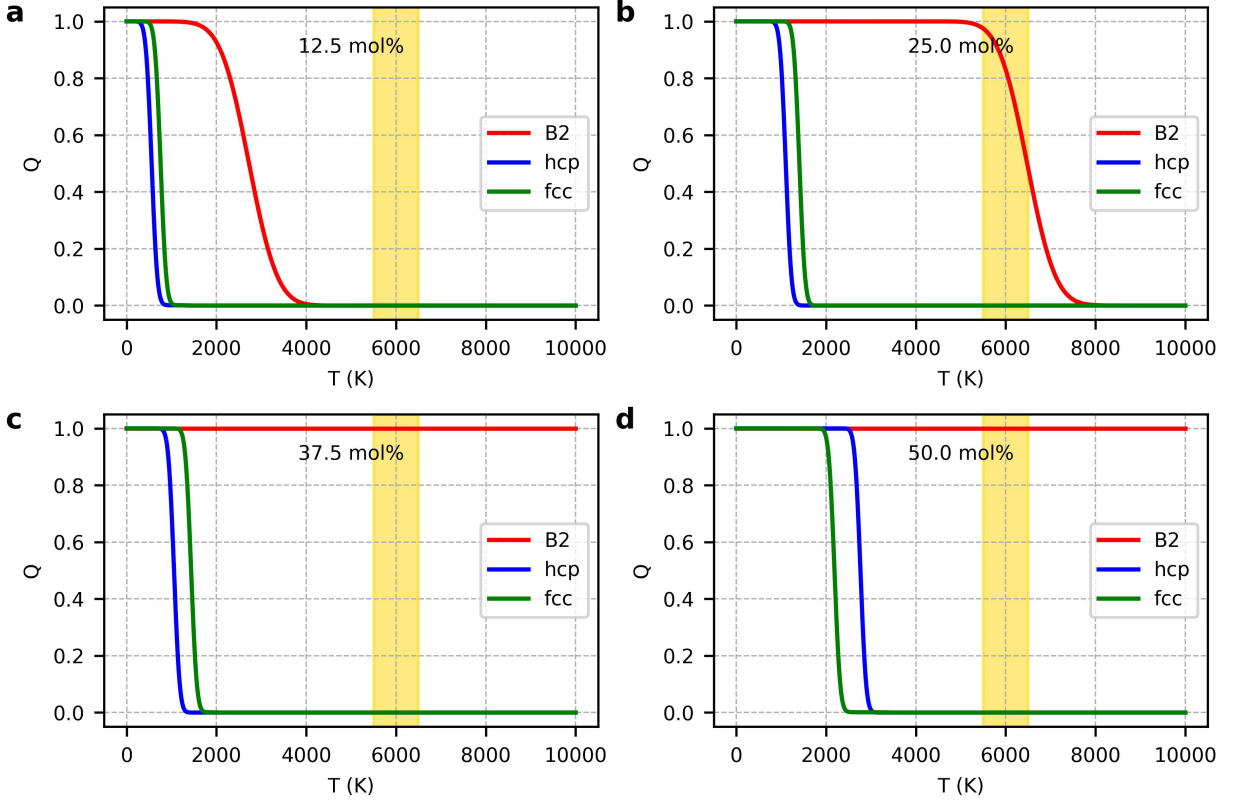


Fig. 2. **Order–disorder phase transition in Fe–Si alloys.** Temperature dependence of the order parameter (Q) for the B2 (red), hcp (blue), and fcc (green) phases of Fe–Si alloys at Si content of **a** 12.5, **b** 25.0, **c** 37.5, and **d** 50 mol%, corresponding to $\text{Fe}_{0.875}\text{Si}_{0.125}$, $\text{Fe}_{0.75}\text{Si}_{0.25}$, $\text{Fe}_{0.625}\text{Si}_{0.375}$, and $\text{Fe}_{0.5}\text{Si}_{0.5}$, respectively. The yellow shaded region indicates the estimated temperature range of Earth’s inner core [5]. The disordered phase ($Q = 0$) of the B2 phase corresponds to the bcc structure.

and S_{vib} is the vibrational entropy, all obtained from FPMD simulations at fixed temperature. Different supercell configurations corresponding to Q values between 0 and 1 were generated to capture the full order–disorder phase relationship (see Methods). The enthalpy of the B2 structure (Fig. 1a) indicates that Si atoms preferentially occupy one of the two sublattice sites in the two-site model ($Q = 1$), rather than being equally distributed between the two sites as in the disordered state ($Q = 0$). The disordered configuration exhibits substantially higher total entropy, with approximate contributions of $0.10 k_B$ from configurational and $0.05 k_B$ from vibrational sources. Consequently, the Gibbs free energy curves (Fig. 1d) indicate that $\text{Fe}_{0.875}\text{Si}_{0.125}$ favors the disordered bcc state over the ordered B2 phase by ~ 41 meV per atom at 330 GPa and 6000 K.

The competition between configurational entropy and interatomic interactions governs the degree of Fe–Si ordering. Configurational entropy favors complete disorder, stabilizing the bcc phase in which Si atoms randomly occupy both bcc sublattices with equal probability, consistent with the ideal mixing approximation [28, 55]. This entropic effect becomes increasingly dominant at higher temperatures, driving an order–to–disorder transition that is either continuous or discontinuous depending

on the curvature of the Gibbs free energy surface with respect to Q , P , T , and X . The vibrational entropy, S_{vib} , also depends on Q , so we also computed the vibrational entropy versus Q .

By identifying the local minima of the Gibbs free energy at varying temperatures, we obtained the temperature dependence of the order parameter (Q) for the B2, hcp, and fcc phases of Fe–Si alloys with different compositions (Fig. 2). At 12.5 mol% Si, the B2, hcp, and fcc phases all become disordered under inner-core temperatures. Specifically, the B2 phase transforms into a fully disordered bcc structure above ~ 4000 K at 330 GPa, fig:bcc and the hcp and fcc phases undergo disordering at much lower temperatures, near 1000 K. The transition temperature systematically increases with Si content; the B2 phase remains ordered even at 6000 K for Si concentrations exceeding 25 mol%. In contrast, both hcp and fcc Fe–Si alloys remain disordered across the entire composition range (0–50 mol%) at 330 GPa and 6000 K.

The disordered bcc phase of Fe–Si alloys is stabilized only at high temperatures, whereas the ordered B2 structure has been consistently observed in X-ray diffraction (XRD) experiments [35]. Our calculated XRD patterns for Fe–Si alloy at 330 GPa and 6000 K (Fig. S3 in the

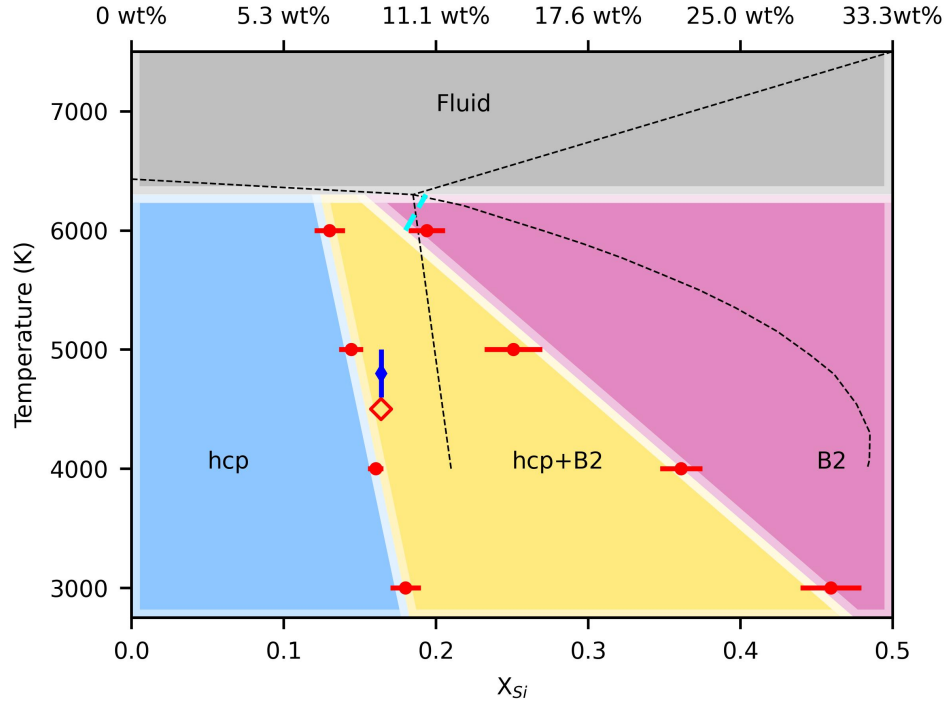


Fig. 3. **Composition-temperature phase diagram of Fe-Si alloys at 330 GPa.** Red points denote phase boundaries separating hcp (blue), coexisting hcp+B2 (yellow), and B2 (magenta) regions, determined from common-tangent constructions between Gibbs free energy curves of the B2 and hcp phases at different temperatures. The ordered B2-Fe-Si alloy transforms into a disordered bcc phase ($Q = 0$) above the dashed cyan line. The dashed black lines represent the phase boundaries (hcp, coexistence, B2, and fluid) determined in Ref. 45. The shaded grey regions indicate the constraints imposed by melting curves beyond the range of our simulations. The blue diamond indicates the experimental constraints [36] defining the boundary between the hcp phase and the hcp/B2 mixture for Fe-9Si at 330 GPa. The open red diamond is extrapolated from lower-pressure experiments [35].

Supplemental Materials) show that the bcc phase is characterized by a set of reflections (e.g., $\langle 110 \rangle$, $\langle 200 \rangle$), and the ordered B2 phase exhibits additional peaks (e.g., $\langle 100 \rangle$, $\langle 111 \rangle$, and $\langle 210 \rangle$). According to Bragg's law ($n\lambda = 2d\sin\theta$), the bcc peaks shift to smaller diffraction angles relative to those of the B2 phase, reflecting the volume expansion accompanying disorder. This shift arises from increased interatomic spacing as Si atoms become randomly distributed in the disordered bcc lattice. The loss of long-range order thus reduces packing efficiency and weakens directional bonding, leading to a modest lattice expansion of the disordered bcc phase.

We constructed Gibbs free energy curves for varying Si composition within the relevant crystalline phases, including B2, hcp, fcc, and bcc (Fig. S4 in the Supplemental Materials). Naturally, pure Fe lacks a configurational entropy contribution because there is no compositional disorder. The hcp Fe remains the most thermodynamically stable phase across the studied temperature range. With increasing temperature, the free energy difference between the hcp and bcc iron progressively decreases, due to the higher vibrational entropy of the bcc phase relative to hcp Fe, consistent with previous studies [9, 56].

In the $\text{Fe}_{0.5}\text{Si}_{0.5}$ alloy, the ordered B2 phase is thermo-

dynamically more stable than the hcp and fcc structures at low temperatures, primarily due to its lower internal energy (Fig. S4 in the Supplemental Materials). However, the B2 phase exhibits substantially lower configurational and vibrational entropy than the disordered bcc solid solution. Although the hcp phase is energetically less favorable at low temperatures, it has greater atomic disorder and, correspondingly, larger entropy contributions. As temperature increases, these entropic effects progressively narrow the free-energy gap between the ordered B2 phase and other disordered phases, such as the hcp phase.

At intermediate Si contents (0–50 mol%), the Gibbs free energy landscape is strongly influenced by the order-disorder transition within the B2 structure. For Si concentrations below 12.5 mol%, the Gibbs free energies of the B2 and bcc phases converge, indicating an order-disorder transition from B2 to bcc. Meanwhile, the free energy of the B2 $\text{Fe}_{0.875}\text{Si}_{0.125}$ becomes comparable to that of the hcp and fcc phases above 5000 K, highlighting the thermodynamic competition among these structures at elevated temperatures. In contrast, for Si content exceeding 25 mol%, no clear order-disorder transition is observed in the B2 phase up to 6000 K (Fig. 2). The

fully ordered B2 phase ($Q = 1$) exhibits substantially lower configurational and vibrational entropies (Fig. S5 and S6 in the Supplemental Materials) than the hcp and fcc phases, which remain disordered ($Q = 0$). Consequently, the free energy difference between the B2 and hcp phases decreases with increasing temperature.

Using the composition-dependent Gibbs free energy curves, we constructed the Fe–Si binary phase diagram through common tangent constructions between competing phases (Fig. 3). At each temperature, the two common tangent points define the boundaries separating single- and two-phase regions. The resulting phase diagram reveals three distinct compositional regimes: a low-Si hcp phase, an intermediate two-phase field comprising hcp, B2, and bcc phases, and a high-Si B2 stability region. At 3000 K, the Fe–Si system exhibits a pronounced miscibility gap between the hcp and B2 phases, allowing their coexistence across a broad compositional range of approximately 16–46 mol% Si. Both boundaries of the two-phase region show negative slopes with respect to temperature, reflecting the higher total entropy of the B2 and bcc phases compared to the hcp phase, consistent with Fe–Si and Fe–Ni–Si alloy experiments at lower pressures [35, 37]. The steep, low-Si boundary coincides with the experimentally determined Fe–9 wt% Si phase boundary at 330 GPa [36], in contrast to the more gradual evolution of the high-Si boundary. This asymmetry arises from differences in entropy and enthalpy contributions across the composition range: at low Si contents, the disordered B2 phase ($Q = 0$, bcc) possesses higher entropy and enthalpy than the hcp phase, whereas at high Si contents, the ordered B2 phase ($Q = 1$, B2) exhibits lower entropy and enthalpy. These opposing trends result in a progressive narrowing of the miscibility gap as the temperature increases.

The low-Si boundary of the miscibility gap is well described by a linear fit, whereas the high-Si boundary exhibits larger uncertainty. This asymmetry arises from both numerical and thermodynamic factors. At low Si contents, the Gibbs free energy curve of the hcp phase displays large curvature (Fig. S4 in the Supplemental Materials), making the tangent point well defined and relatively insensitive to small compositional fluctuations. In contrast, the Gibbs free energy surface of the high-Si B2 phase is much flatter due to its lower configurational entropy and weaker compositional dependence, resulting in smaller curvature and, consequently, greater uncertainty in the tangent construction. Because the positions of the two tangent points are coupled through the common tangent condition, any minor deviation in the low-Si region propagates to the high-Si boundary, amplifying its uncertainty. This effect is further enhanced by the finite configurational sampling of the 128-atom supercell used in this study. This entropy difference raises the melting temperature due to the order–disorder transition.

Furthermore, the core temperature is influenced by the melting behavior of Fe–Si alloys. In the case of disordered bcc $\text{Fe}_{0.875}\text{Si}_{0.125}$ ($Q = 0$), both vibrational and

configurational entropies (Fig. 1b and c) are elevated by $0.05 k_B$ and $0.10 k_B$, respectively, relative to the fully ordered B2 phase ($Q = 1$). This increase in entropy implies that the order–disorder transition raises the melting temperature of the Fe–Si alloy compared to the ordered configurations typically assumed in earlier melting studies [57]. Consequently, this effect may play an important role in shaping the thermal evolution and crystallization history of Earth’s early core.

DISCUSSION

Phase Diagram Comparison

We observe several key differences between our phase diagram and that of Ref. 45, who employed hybrid Monte Carlo simulations with deep-learning interatomic potentials. Firstly, our results reveal a B2–hcp two-phase coexistence field that extends to lower Si concentrations (approximately 12–16 mol%) across the 3000–6000 K range. In contrast, their phase diagram locates the corresponding hcp–B2 boundary at significantly higher Si content (~ 20 mol%). We attribute this discrepancy to challenges in achieving equilibrium at low Si concentrations in semi-grand-canonical Monte Carlo simulations, which can lead to misplacement of phase boundaries.

Secondly, our results differ in the nature of the bcc–B2 transition. Ref. 45 reported a persistent miscibility gap between a short-range-ordered bcc phase and a long-range-ordered B2 phase. This gap expands upon cooling and remains open even at 0 K, indicating a first-order transition. In contrast, our calculations reveal no such coexistence region: the bcc phase transforms continuously into the B2 phase at low Si concentration (Fig. S7). The Gibbs free energy curves for bcc and B2 merge smoothly over the entire 3000–6000 K temperature range (Fig. S4), suggesting a second-order (continuous) transformation. Furthermore, the bcc–B2 boundary in our study occurs at significantly lower Si concentrations than in their phase diagram, explaining the lower miscibility gap boundary shown in Fig. 3.

Thirdly, analysis of the chemical potential (Fig. S8, Eq. 6) further supports this continuous transition. The chemical potential curves for B2 and bcc phases merge smoothly at low Si concentrations ($\sim 12.5\%$), in contrast to the discontinuous behavior implied by a first-order transition in Ref. 45. Minimal numerical errors could give rise to an apparent miscibility gap. Although both studies show good agreement for the hcp and B2 phases at higher Si content, our Gibbs free energy profile exhibits a steeper negative slope in the low-Si region.

Furthermore, compared to Ref. 45, we identify a narrower miscibility gap, shifted toward lower Si concentrations, and a distinct bcc stability pocket emerging above 5100 K—substantially below the 6000 K onset predicted in their work at ~ 20 mol% Si. These differences cannot be due to short-range order, which is not included in our

study, because short-range order would stabilize B2/bcc relative to hcp, whereas the opposite is observed in their results.

Our results are broadly consistent with experimental constraints on Fe–Si alloys at high pressure [35, 36], but the experiments do not resolve the slope of the hcp–B2 phase boundary because only a single Si concentration (Fe–9 wt% Si, i.e. 16 mol%) has been measured at inner-core pressures. Fischer *et al.* mapped the Fe–Si phase diagram only up to 145 GPa, and thus cannot provide constraints at 330 GPa. By extrapolation to 330 GPa, we find that for Fe–9 wt% Si the B2 phase becomes competitive with hcp above 4500 K, in agreement with the experimental observation that Fe–9 wt% Si remains in the hcp structure up to 4800 K before transforming [36]. Although experiments provide only a single composition point, our results suggest that the coexistence and hcp–B2 transition boundaries extend to higher Si contents than previously inferred.

B2 phase stability

Although silicon has long been recognized as a primary light element in Earth’s core [31], recent estimates based on the stability of the hcp phase [26, 32] suggest an abundance of approximately 2.3–4.1 wt.% (4.5–7.9 mol.%). According to our composition–temperature phase diagram, a disordered bcc-structured Fe–Si alloy is not thermodynamically stable under inner core conditions at equilibrium, implying that the hcp phase should remain the predominant solid structure in a fully equilibrated system under these pressure and temperature conditions.

From a dynamic perspective of core cooling, however, the B2 phase may play a crucial role during the nucleation stage of inner core crystallization. Yang Sun *et al.* [11] demonstrated that the metastable bcc phase of iron exhibits significantly higher nucleation rates than the hcp phase under inner core conditions. This two-step nucleation mechanism, in which bcc forms first and subsequently transforms into hcp, reduces the undercooling required for solidification and provides a plausible solution to the so-called inner core nucleation paradox.

Furthermore, experimental evidence [41] indicates that hydrogen markedly enhances the silicon concentration in B2 crystals, increasing the Si/Fe molar ratio to approximately 1, and B2 crystals mostly remain in the coexisting Fe liquid. The resulting Si-rich B2 phase is stabilized in solid form at outermost core temperatures and is less dense than the surrounding liquid, enabling it to float upward and accumulate near the core–mantle boundary (CMB). These dynamic processes underscore the importance of investigating Fe–Si alloys with higher silicon contents. To assess the stability of these compositions, we compared the Gibbs free energy of a mechanical mixture of pure B2 FeSi and pure hcp Fe with that of hcp and B2 Fe–Si alloy (Fig. S4 in the Supplemental Materials). At 3000 K, the free energy of the FeSi + Fe mixture

is only slightly higher than that of the hcp + B2 alloy. However, this difference increases with temperature, indicating that pure B2 FeSi is not stable under inner core conditions.

These combined thermodynamic, kinetic, and chemical considerations imply that, although the hcp phase dominates at equilibrium, the bcc and B2 phases likely play important transitional roles during core cooling and could leave observable signatures in seismic observations. The presence of disordered bcc-structured Fe–Si alloys can substantially influence the physical properties of the inner core, particularly its thermal conductivity and seismic velocities. Such effects provide a plausible explanation for key geophysical observations, including the pronounced seismic anisotropy [20] and relatively low thermal conductivity [58] inferred for the inner core. The intrinsic shear anisotropy (A_{cb}) of the bcc structure could contribute to the observed seismic anisotropy patterns, and the disordered distribution of silicon atoms in the B2 lattice can reduce electronic thermal conductivity through enhanced electron scattering. Together, these mechanisms suggest that metastable bcc-structured Fe–Si alloys may have exerted a lasting influence on the seismic and thermal evolution of Earth’s inner core.

Transport properties

We calculated the electrical transport properties of $\text{Fe}_{0.875}\text{Si}_{0.125}$ alloy in both B2 and hcp structures at 330 GPa and 6000 K, corresponding to Earth’s inner core (IC) conditions (Fig. 4). Previous experiments [58] demonstrated that Si doping substantially increases the electrical resistivity of pure iron through enhanced impurity scattering. Similarly, the order–disorder transition in $\text{Fe}_{0.875}\text{Si}_{0.125}$ alloys further amplifies scattering effects, leading to higher resistivity. Varying the order parameter Q and crystal structure reveals that the total electronic density of states (DOS) near the Fermi level changes only slightly (Fig. 4d), yet electrical and thermal transport exhibit strong sensitivity to atomic ordering. Both resistivity and thermal conductivity vary systematically with Q : resistivity decreases and thermal conductivity increases as the degree of order rises from $Q = 0$ to $Q = 1$ (Fig. 4a,b). At 6000 K, the ordered B2 structure exhibits a slightly higher resistivity ($\sim 2.0 \mu\Omega\cdot\text{cm}$) and lower thermal conductivity ($\sim 13 \text{ W m}^{-1} \text{ K}^{-1}$) than the hcp structure. The order–disorder transition decreases resistivity by $\sim 1.8\text{--}4.0 \mu\Omega\cdot\text{cm}$ and increases thermal conductivity by $\sim 3.8\text{--}4.5 \text{ W m}^{-1} \text{ K}^{-1}$ for both B2 and hcp structures, respectively. The resulting Lorenz number of $\sim 2.1\text{--}2.2 \times 10^{-8} \text{ W}\Omega \text{ K}^{-2}$ agrees well with theoretical expectations (Fig. 4c). For comparison, previous work [59] estimated a thermal conductivity of $\sim 190 \text{ W m}^{-1} \text{ K}^{-1}$ for FeH_x alloys under IC conditions, similar to that of the ordered hcp $\text{Fe}_{0.875}\text{Si}_{0.125}$ alloy ($\sim 183.7 \text{ W m}^{-1} \text{ K}^{-1}$). In contrast, the disordered bcc $\text{Fe}_{0.875}\text{Si}_{0.125}$ alloy has a

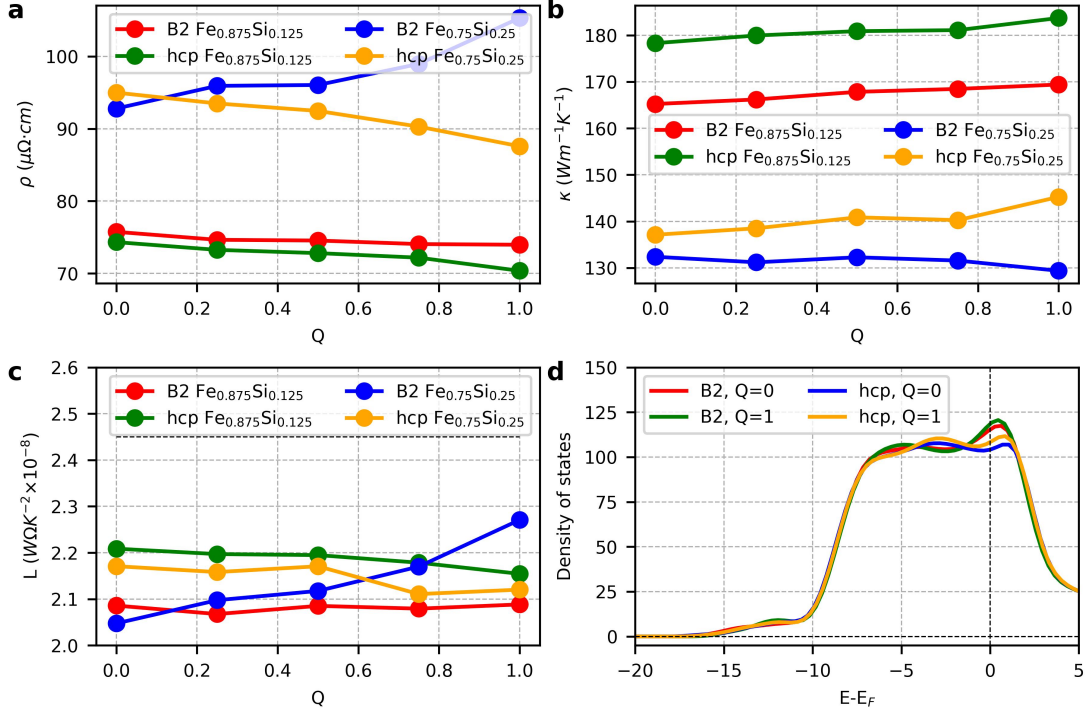


Fig. 4. **Electrical transport properties of Fe-Si alloys at ~330 GPa and 6000 K.** **a** Electrical resistivity (ρ), **b** thermal conductivity (κ), and **c** Lorenz number (L) for B2 and hcp Fe-Si alloys with Si contents of 12.5 mol% and 25 mol% ($\text{Fe}_{0.875}\text{Si}_{0.125}$ and $\text{Fe}_{0.75}\text{Si}_{0.25}$). The order parameter Q varies from 0 (bcc, disordered) to 1 (B2, ordered). The ideal Lorenz number ($L_0 = 2.45 \times 10^{-8} \text{ W}\Omega\text{K}^{-2}$) is indicated by the dotted horizontal line. **d** Total electronic density of states (DOS) of $\text{Fe}_{0.875}\text{Si}_{0.125}$, with the Fermi energy shifted to zero. In the B2 structure, $\text{Fe}_{0.875}\text{Si}_{0.125}$ stabilizes in the disordered ($Q = 0$, bcc-like) phase, while $\text{Fe}_{0.75}\text{Si}_{0.25}$ remains ordered ($Q = 1$) at 6000 K.

lower thermal conductivity of $\sim 165.2 \text{ W m}^{-1} \text{ K}^{-1}$, about 7% less than that of the disordered hcp phase.

We also conducted transport property calculations for the higher-silicon composition $\text{Fe}_{0.75}\text{Si}_{0.25}$, with results shown in Fig. 4. Increasing the silicon content from $\text{Fe}_{0.875}\text{Si}_{0.125}$ to $\text{Fe}_{0.75}\text{Si}_{0.25}$ induces pronounced changes in electronic transport behavior. The electrical resistivity increases substantially, while the thermal conductivity decreases by more than $\sim 40 \text{ W m}^{-1} \text{ K}^{-1}$, representing a reduction of about 30% compared with the lower-silicon alloy. Notably, the relationship between electrical resistivity and the order parameter Q differs between structures: in the B2 phase, resistivity decreases with increasing Q (a positive correlation), whereas in the hcp phase, it shows a weak negative correlation. This contrasting behavior highlights the interplay between chemical disorder and crystal symmetry in the transport properties of Fe-Si alloys under inner-core conditions.

Electrical and thermal conductivities of iron alloys in the core are critical for constraining Earth's thermal evolution and the behavior of the geodynamo. Higher conductivities imply more efficient heat transfer, which accelerates core cooling and shortens the timescale for inner core growth. Accounting for the disordered bcc Fe-Si alloy, which exhibits reduced thermal conductivity, our results indicate a slower core cooling rate and,

consequently, a potentially lower core temperature in the early Earth. At higher silicon contents, the B2 phase becomes more stable than the bcc phase; moreover, B2 Fe-Si alloys typically have thermal conductivities $\sim 15 \text{ W m}^{-1} \text{ K}^{-1}$ lower than those of the hcp phase. The markedly reduced thermal conductivity of $\text{Fe}_{0.75}\text{Si}_{0.25}$, combined with the potential development of a B2-rich shell surrounding an hcp Fe-Si inner core, could introduce an additional thermal barrier that impedes heat flux from the core. Such a layered structure would moderate core heat loss, reconcile discrepancies in current core-cooling models, and help sustain Earth's magnetic field over geological timescales.

Seismic properties

In addition to electrical transport properties, the crystal structure (B2 vs. hcp) also has a strong influence on the elastic constants and seismic velocities of Fe-Si alloys under inner core (IC) conditions. The calculated elastic constants (C_{ij}) decrease systematically with increasing temperature. Although both structures exhibit comparable bulk moduli, the disordered bcc ($Q = 0$) $\text{Fe}_{0.875}\text{Si}_{0.125}$ alloy possesses a substantially lower shear modulus than the hcp phase, resulting in significantly reduced shear

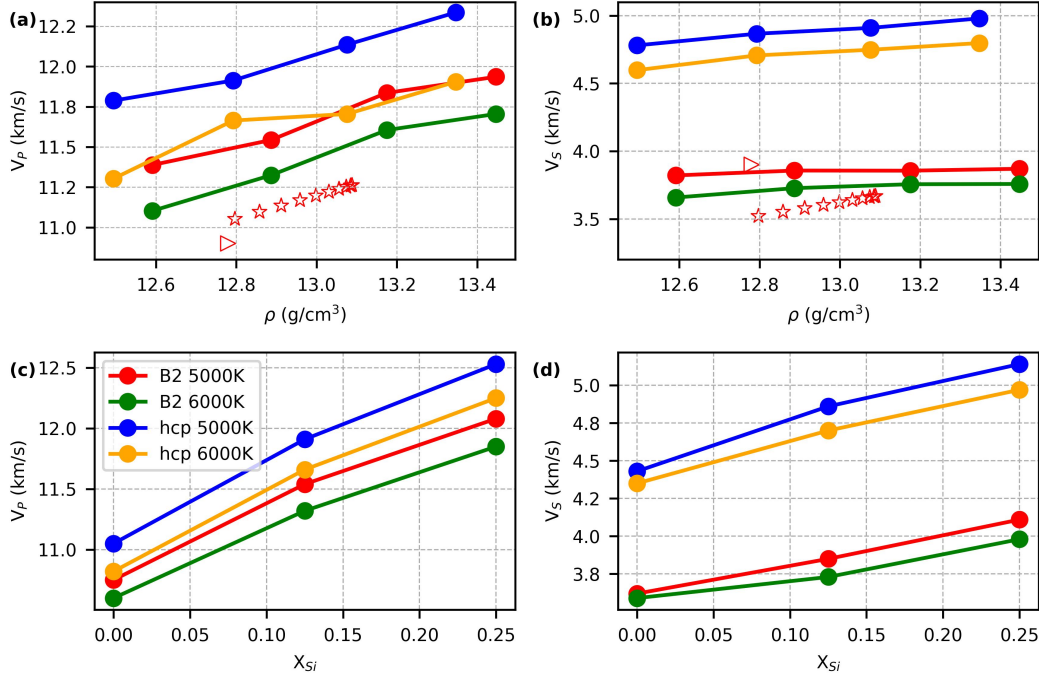


Fig. 5. **Seismic velocities of Fe–Si alloys as a function of density and composition.** Calculated compressional-wave (V_P) and shear-wave (V_S) velocities of $\text{Fe}_{0.875}\text{Si}_{0.125}$ alloys in the B2 (a) and hcp (b) phases are compared with the Preliminary Reference Earth Model (PREM) [60] values for the inner core (open red stars) and with previous simulations (open triangles)[45]. Panels (c) and (d) show the composition dependence of seismic velocities for B2 and hcp phases at 5000 K and 6000 K, including pure Fe, $\text{Fe}_{0.875}\text{Si}_{0.125}$, and $\text{Fe}_{0.75}\text{Si}_{0.25}$. In the B2 structure, $\text{Fe}_{0.875}\text{Si}_{0.125}$ is stabilized in the disordered ($Q = 0$, bcc-like) phase, whereas $\text{Fe}_{0.75}\text{Si}_{0.25}$ remains ordered ($Q = 1$) at 5000 K and 6000 K.

wave velocities under IC conditions (Table S2 in the Supplemental Materials).

The origin of seismic anisotropy in Earth’s inner core remains debated, with recent studies proposing diverse mechanisms to explain the observed seismic signatures. The interplay between seismological observations and mineral physics models suggests that inner-core anisotropy may arise from depth-dependent phase transitions, shear softening, and variations in light-element composition [61–67]. Consistent with previous results for pure hcp Fe [20], our calculations show that the elastic anisotropy of hcp Fe–Si alloys is nearly zero under inner-core conditions, indicating that the hcp phase alone cannot account for the observed seismic anisotropy of Earth’s inner core.

We computed the directional dependence of elastic anisotropy for $\text{Fe}_{0.875}\text{Si}_{0.125}$ at 5000 K and 6000 K (Fig. S9 in the Supplemental Materials). For both compressional and shear waves propagating along different orientations relative to the c -axis, the B2 structure exhibits stronger velocity variations than the hcp phase. At 6000 K, the shear wave velocity in B2 Fe–Si ranges from ~ 2.4 to 5.0 km/s, corresponding to a pronounced Chung–Buessem shear anisotropy of 22.9%, compared with only 0.6% for the hcp phase. These values represent ideal single-crystal limits; in the real inner core,

polycrystalline averaging due to solidification and plastic deformation would substantially reduce the observable anisotropy. Nevertheless, the intrinsically higher anisotropy of the B2 structure suggests that even partial crystallographic alignment during inner-core growth could produce the seismic anisotropy detected in observations. Together, these results suggest that B2 Fe–Si alloys—stabilized by elevated temperature and silicon enrichment—may play a crucial role in reconciling mineral physics predictions with the observed seismic anisotropy of Earth’s inner core.

The compressional (V_P) and shear (V_S) wave velocities of disordered B2 and hcp $\text{Fe}_{0.875}\text{Si}_{0.125}$ alloys were calculated at varying densities using their elastic constants, as shown in Fig. 5 a,b. Both V_P and V_S increase with density, consistent with the effects of compression. Previous studies [45] reported a V_S of 3.93 km/s at 12.78 g/cm³ for a short-range ordered stabilized bcc Fe–Si alloy, slightly higher than our calculated value of 3.73 km/s. Notably, the V_S curve of the B2 phase at 6000 K aligns more closely with the PREM model than that of the hcp phase, suggesting that the B2 structure—potentially stabilized by silicon incorporation—is a compelling candidate for the dominant Fe-bearing phase in Earth’s inner core. The pressure dependence of seismic velocities is shown in Fig. S10 of the Supplemental Materials.

Beyond $\text{Fe}_{0.875}\text{Si}_{0.125}$, we extended our investigation to pure Fe and $\text{Fe}_{0.75}\text{Si}_{0.25}$ compositions at 5000 K and 6000 K (Fig. 5 c,d). Both V_P and V_S increase approximately linearly with silicon content, consistent with previous experimental and theoretical studies [26]. By interpolating to the geophysically plausible Si range of 4.5–7.9 mol% [26, 32], we estimate shear-wave velocities at the inner-core boundary (ICB) of 3.68–3.70 km/s for the B2 phase and 4.64–4.67 km/s for the hcp phase. The hcp values are notably higher than the PREM shear velocity of ~ 3.6 km/s, reinforcing the long-recognized discrepancy between seismological observations and models based solely on hcp phase.

We further derived Poisson’s ratio from the calculated V_P and V_S values (Fig. S11 in the Supplemental Materials). The density- and composition-dependent Poisson’s ratio of the bcc-like $\text{Fe}_{0.875}\text{Si}_{0.125}$ alloy is significantly higher than that of the hcp phase and closely matches seismological estimates ($\nu = 0.44$) [60]. In particular, the B2 phase exhibits a V_P/V_S ratio of ~ 3.0 and a Poisson’s ratio of ~ 0.44 , about 20% and 10% greater than those of the hcp phase, respectively. Previous studies [26, 63, 68] constrained the silicon content of the inner core to relatively low values, assuming that Si is incorporated only into hcp Fe alloys. However, the hcp Fe–Si phase alone cannot reproduce the observed high V_P/V_S ratio. Our results therefore suggest that incorporating the B2 Fe–Si phase yields somewhat higher Si concentrations in the inner core, while remaining consistent with seismological constraints.

Overall, our extended calculations demonstrate that across a wide range of compositions and temperatures, B2 Fe–Si alloys exhibit seismic properties that are much closer to the PREM model than those of their hcp counterparts. The order–disorder transition inherent to the B2 structure naturally reduces V_S while increasing the V_P/V_S ratio, providing a plausible explanation for the seismic softness of Earth’s inner core. We therefore propose that the stabilization of the B2 phase by silicon, and its associated order–disorder behavior, offer a robust alternative to the superionic model [69] for reconciling mineral-physics predictions with the observed low shear-wave velocities of the inner core.

Furthermore, seismic studies reveal the existence of an “innermost inner core” (IIC), extending from approximately 300 to 750 km in radius, which exhibits anisotropy nearly 70% stronger than that of the overlying inner core [70, 71]. Recent work suggests that molten iron may crystallize under core conditions through a two-step nucleation mechanism involving metastable bcc precursors [11]. This mechanism significantly reduces the undercooling required for solidification and may influence the structural evolution of the inner core. Importantly, our phase diagram (Fig. 3) indicates that the B2/bcc phase becomes increasingly stabilized relative to hcp toward the core center temperature, with silicon incorporation further enhancing this effect. The persistence of a bcc-dominated region in the innermost core could therefore

account for the pronounced anisotropy of the IIC, as the B2/bcc phase possesses substantially higher intrinsic shear anisotropy than hcp. These results suggest that at least two solid phases, hcp and B2/bcc, likely coexist in Earth’s core at realistic Si contents. Spatial variations in anisotropy within the inner core may thus arise from compositional differences in silicon, leading to varying proportions of hcp and B2 phases, as well as from textural evolution associated with flow and crystallization history.

In summary, we constructed a two-site model to generate a series of configurations ranging from ordered to disordered states across varying silicon contents in Fe–Si alloys. First-principles calculations reveal an order–disorder transition in alloys with Si contents below 25 mol%, arising from the interplay of enthalpy, configurational entropy, and vibrational entropy in the Gibbs free energy. Based on these results, we established the Fe–Si binary phase diagram from 3000 to 6000 K and identified a wide B2-hcp coexistence field under Earth’s inner core (IC) conditions. The B2 Fe–Si alloy moderately affects electrical transport properties, such as electrical resistivity and thermal conductivity, as well as seismic wave velocities. These findings carry significant geophysical implications: the reduced thermal conductivity of the B2 phase may slow inner-core cooling and imply an older inner-core age. At the same time, its lower shear-wave velocity and pronounced elastic anisotropy are consistent with seismic observations, supporting the coexistence of B2 and hcp Fe–Si phases within Earth’s inner core.

METHODS

Configuration generation

To investigate the order–disorder phase transition in Fe–Si alloys, we introduced an order parameter Q within a two-site model framework for bcc, hcp, and fcc structures (Fig. S1 in the Supplemental Materials). The order parameter quantifies the degree of chemical ordering and is defined as follows:

$$Q = \frac{\sum_i |C_i^{\text{struct}} - C_i^{\text{random}}|}{\sum_i |C_i^{\text{random}}|}, \quad (3)$$

where C_i^{struct} and C_i^{random} represent the correlation functions for a given structure and for a perfectly random alloy, respectively. Here, $Q = 0$ corresponds to a fully disordered configuration with Si atoms equally distributed between both sites, while $Q = 1$ denotes a fully ordered phase with Si atoms occupying only one sublattice.

We generated Q -dependent atomic configurations using the Alloy Theoretic Automated Toolkit (ATAT) with the Special Quasirandom Structure (SQS) method [72]. An SQS is a finite periodic supercell that approximates the correlation functions (pairs, triplets, etc.) of a perfectly random alloy within a limited number of atoms.

Pair clusters up to the second, third, and fourth nearest neighbors (cutoff distances 2.5, 3.0, and 3.5 Å) were included, and the deviation from random correlation functions was minimized. The SQS thus provides a reproducible and efficient representation of chemical disorder, enabling accurate evaluation of thermodynamic and electronic properties while capturing local lattice distortions.

For each target order parameter Q , we constructed a 128-atom ($4 \times 4 \times 4$) supercell for the bcc, hcp, and fcc lattices. The procedure included: (i) defining the parent lattice and atomic basis in a VASP-compatible POSCAR; (ii) specifying the target composition; (iii) performing Monte Carlo sampling to generate candidate configurations; (iv) evaluating the deviation of correlation functions from random values; and (v) selecting the configuration with the lowest score as the representative SQS. The SQS quality was validated by comparing short-range pair and multi-site correlations to those of a random alloy.

We systematically varied Q from 0 to 1 for each structure type and Si concentration, using 5, 5, 4, and 5 intermediate Q values for Si = 12.5, 25.0, 37.5, and 50.0 mol%, respectively. Atomic occupation details for each configuration are listed in Table S1 of the Supplemental Materials.

The configurational entropy S_{conf} was calculated as

$$\frac{S_{\text{conf}}}{k_B} = - \sum X \ln X, \quad (4)$$

where X is the site occupation probability of Fe or Si and k_B is Boltzmann's constant. At a fixed composition, S_{conf} decreases monotonically as Q increases from 0 to 1. The entropy difference between ordered and disordered states depends strongly on Si concentration (Fig. S5 in the Supplemental Materials).

Convergence tests using larger supercells (up to 200 atoms) confirmed that both the free energy and order parameter Q converge within statistical uncertainty, indicating that a 128-atom supercell provides a reliable representation of the disordered phase (Fig. S12 in the Supplemental Materials). Specifically, for $\text{Fe}_{0.5}\text{Si}_{0.5}$ at 330 GPa, the enthalpy decreases from the disordered bcc phase ($Q = 0$) toward the ordered B2 phase ($Q > 0$), with larger supercells improving convergence, particularly at lower Q . Molecular dynamics simulations of the disordered bcc structure at 6000 K show that the Gibbs free energy plateaus beyond 108 atoms, with variations within 10 meV/atom between 128 and 200 atoms. Thus, the 128-atom supercell offers a robust compromise between accuracy and computational efficiency.

First-principles calculations

The optimal SQS structure, corresponding to the minimum value of the objective function, was optimized at 330 GPa through full relaxation of both lattice parameters and atomic positions. For the bcc and fcc structures,

the cell shape was constrained by fixing the lattice constants such that $a = b = c$, whereas for the hcp structure, the c/a ratio was allowed to relax.

Density functional theory (DFT) calculations were performed using the Vienna *Ab initio* Simulation Package (VASP) [73]. The projector augmented-wave (PAW) method [74] was employed together with the generalized gradient approximation (GGA) using the Perdew–Burke–Ernzerhof (PBE) exchange–correlation functional [75]. The $3s^23p^64s^23d^6$ electrons in Fe and the $3s^23p^2$ electrons in Si were treated as valence electrons. A plane-wave energy cutoff of 500 eV was adopted, and Brillouin-zone integrations were carried out using a $2 \times 2 \times 2$ Monkhorst–Pack k -point mesh. The total energy convergence threshold for structural relaxation was set to 10^{-6} eV.

First-principles molecular dynamics simulations

To account for the vibrational entropy of Fe–Si alloys (128 atoms) under high-pressure and high-temperature conditions, first-principles molecular dynamics (FPMD) simulations were performed based on the Born–Oppenheimer approximation, as implemented in VASP. The Perdew–Burke–Ernzerhof (PBE) exchange–correlation functional within the generalized gradient approximation was employed, with Brillouin-zone sampling restricted to the Γ point. A plane-wave energy cutoff of 500 eV was used, ensuring total-energy convergence better than 10^{-5} eV.

Equilibrium volumes at different temperatures were determined by conducting NPT simulations over a grid of temperatures at 330 GPa, using a Langevin thermostat [76] to control temperature. Each molecular dynamics simulation was run for 6 ps with a time step of 1.0 fs, of which the first 1 ps was discarded for equilibration. Data from the remaining 5 ps were used to compute ensemble-averaged properties. The internal energies of Fe–Si alloys at various temperatures were obtained from these averages, and the associated uncertainties were propagated through the construction of common tangents on the Gibbs free energy curves, thereby constraining the phase boundaries (Fig. 3).

Chemical potential calculations

To represent the composition- and temperature-dependent Gibbs free energy of the Fe–Si system, we adopted a combined polynomial–logarithmic expression:

$$\begin{aligned} G(X, T) &= a + bX + cX^2 + dX^3 + eX^4 \\ &\quad + k_B T [X \ln X + (0.5 - X) \ln(0.5 - X)] \end{aligned} \quad (5)$$

In this formulation, X denotes the atomic fraction of Si (limited to $X \leq 0.5$). The polynomial terms capture

the enthalpic contributions to the free energy, while the logarithmic term describes the ideal configurational entropy of mixing in a binary Fe–Si solution. This model accurately reproduces our computed Gibbs free energy data, with fitting residuals below 1 meV/atom across the sampled temperature and composition range.

The chemical potential difference between Si and Fe is given by:

$$\Delta\mu = \mu_{\text{Si}} - \mu_{\text{Fe}} = \frac{\partial G(X, T)}{\partial X}. \quad (6)$$

Differentiating Eq. 5 with respect to x yields:

$$\Delta\mu = b + 2cX + 3dX^2 + 4eX^3 + RT \ln \left(\frac{X}{1-X} \right). \quad (7)$$

Vibrational density of states and vibrational entropy

The vibrational density of states (VDOS) was obtained from the Fourier transform of the velocity autocorrelation function (VACF) computed from the FPMD trajectories. The VACF is defined as

$$C(t) = \frac{1}{N} \sum_{i=1}^N \langle \mathbf{v}_i(0) \cdot \mathbf{v}_i(t) \rangle, \quad (8)$$

where $\mathbf{v}_i(t)$ is the velocity of atom i at time t , and the average is taken over all N atoms and multiple time origins along the trajectory. The VDOS $g(\omega)$ is then obtained as the Fourier transform of the normalized VACF:

$$g(\omega) = \int_0^\infty C(t) e^{-i\omega t} dt. \quad (9)$$

In practice, the VACF is computed from discretely sampled velocities, and the Fourier transform is evaluated using a fast Fourier transform (FFT). The resulting VDOS is normalized according to

$$\int_0^\infty g(\omega) d\omega = 3. \quad (10)$$

This approach inherently captures anharmonic vibrational effects at finite temperatures, providing a realistic description of lattice dynamics under extreme thermodynamic conditions relevant to the Earth's inner core. The Fe–Si alloys exhibit solid-like atomic motion in all simulations, as indicated by non-diffusive mean-square displacements (MSD; Fig. S13 in the Supplemental Materials). Furthermore, the vanishing low-frequency limit of the VDOS, $g(0) = 0$, confirms the absence of diffusive behavior and the preservation of solid phases.

The vibrational entropy per atom at temperature T is computed under the quasi-harmonic approximation as

$$S_{\text{vib}} = k_B \int_0^\infty g(\omega) \left[\frac{\hbar\omega}{k_B T} \cdot \frac{1}{e^{\hbar\omega/k_B T} - 1} - \ln \left(1 - e^{-\hbar\omega/k_B T} \right) \right] d\omega, \quad (11)$$

where k_B is the Boltzmann constant and \hbar is the reduced Planck constant. This expression accounts for phonon occupation following Bose–Einstein statistics and incorporates the temperature dependence of vibrational entropy.

The zero-point energy (ZPE), arising from quantum zero-point motion, corresponds to the vibrational energy at absolute zero temperature ($T = 0$ K) and is calculated as

$$E_{\text{ZPE}} = \int_0^\infty \frac{1}{2} \hbar\omega g(\omega) d\omega. \quad (12)$$

This quantity represents the residual vibrational energy retained by the atoms due to quantum effects even at 0 K.

Transport property calculations

The electronic transport properties of the CH compound were computed using a modified spin-polarized relativistic Korringa–Kohn–Rostoker (SPR-KKR) code [77, 78]. Four uncorrelated atomic snapshots were randomly selected from *ab initio* molecular dynamics (AIMD) simulations performed under high-pressure and high-temperature conditions.

For each snapshot, a self-consistent field (SCF) calculation was carried out within the framework of density functional theory (DFT), employing a maximum angular momentum cutoff of $l_{\text{max}} = 3$ and 125 k -points in the Brillouin zone. After convergence, the transport properties were evaluated using the Kubo–Greenwood formalism with the same l_{max} , a denser k -point mesh of 216 points, and an energy window of $[-5k_B T, +5k_B T]$ centered around the chemical potential.

The electrical conductivity (σ), resistivity ($\rho = 1/\sigma$), and thermal conductivity (κ) were derived from the transport coefficients \mathcal{L}_{ij} according to

$$\sigma = \mathcal{L}_{11}, \quad \kappa = \frac{1}{eT} \left(\mathcal{L}_{22} - \frac{\mathcal{L}_{12}^2}{\mathcal{L}_{11}} \right), \quad (13)$$

where the transport coefficients are defined as

$$\mathcal{L}_{ij} = (-1)^{i+j} \int d\varepsilon \sigma_{\mu\nu}(\varepsilon - \mu)^{i+j-2} \left(-\frac{\partial f_T(\varepsilon)}{\partial \varepsilon} \right). \quad (14)$$

Here, $f_T(\varepsilon)$ is the Fermi–Dirac distribution at temperature T , and μ is the chemical potential.

The energy-dependent conductivity tensor $\sigma_{\mu\nu}(\varepsilon)$ was evaluated from the Kubo–Greenwood expression,

$$\sigma_{\mu\nu} \propto \text{Tr} \left\langle \hat{j}_\mu \text{Im} G^+ \hat{j}_\nu \text{Im} G^+ \right\rangle, \quad (15)$$

where \hat{j}_μ is the current operator and $\text{Im} G^+$ denotes the imaginary part of the retarded Green's function.

Elastic property calculations

The independent elastic constants C_{ij} ($i, j = 1, 2, \dots, 6$) were determined by applying small finite distortions to the equilibrium structure and solving the linear stress-strain relations. These constants provide the foundation for evaluating the seismic velocities and elastic anisotropy of Fe-Si alloys under Earth's inner-core conditions.

The elastic properties of disordered bcc- and hcp-structured $\text{Fe}_{0.875}\text{Si}_{0.125}$ alloys were computed under high-pressure and high-temperature conditions using first-principles molecular dynamics (FPMD) simulations. For each structure and temperature, the simulations were run for at least 6 ps to achieve equilibrium, after which the stress tensor was averaged over the final 5 ps of the trajectory.

To evaluate the elastic constants, a set of finite strains ε with magnitudes $\delta = 0, \pm 0.005$, and ± 0.01 was applied to the relaxed structures, generated using the VASPKit package [79]. The corresponding stress tensors σ_{ij} were obtained from DFT calculations for each strained configuration. The elastic constants C_{ij} were then derived by linearly fitting the stress-strain data according to the generalized Hooke's law:

$$\sigma_{ij} = \sum_{k,l} C_{ijkl} \varepsilon_{kl}. \quad (16)$$

After obtaining C_{ij} , the bulk modulus K and shear modulus G were evaluated using the Voigt-Reuss-Hill averaging scheme. The compressional (V_P) and shear (V_S) wave velocities were then calculated as

$$V_P = \sqrt{\frac{K + \frac{4}{3}G}{\rho}}, \quad (17)$$

$$V_S = \sqrt{\frac{G}{\rho}}, \quad (18)$$

where ρ is the density at the target pressure.

The Chung-Buessem shear anisotropy factor A_{CB} is defined as

$$A_{CB} = \frac{G_V - G_R}{G_V + G_R}, \quad (19)$$

where G_V and G_R are the Voigt and Reuss averages of the shear modulus, respectively. $A_{CB} = 0$ corresponds to perfect elastic isotropy, while larger values indicate increasing anisotropy. The elastic constants and derived quantities of $\text{Fe}_{0.875}\text{Si}_{0.125}$ at inner-core conditions are listed in Table S2 in the Supplemental Materials.

The Poisson ratio ν was determined from the V_P/V_S ratio as

$$\nu = \frac{0.5 (V_P/V_S)^2 - 1}{(V_P/V_S)^2 + 1}. \quad (20)$$

-
- [1] M. J. Brown, The equation of state of iron to 450 GPa: Another high pressure solid phase?, *Geophysical Research Letters* **28**, 4339 (2001).
 - [2] L. Dubrovinsky, N. Dubrovinskaia, O. Narygina, I. Kantor, A. Kuznetsov, V. B. Prakapenka, L. Vitos, B. Johansson, A. S. Mikhaylushkin, S. I. Simak, and I. A. Abrikosov, Body-Centered Cubic Iron-Nickel Alloy in Earth's Core, *Science* **316**, 1880 (2007).
 - [3] A. S. Mikhaylushkin, S. I. Simak, L. Dubrovinsky, N. Dubrovinskaia, B. Johansson, and I. A. Abrikosov, Pure Iron Compressed and Heated to Extreme Conditions, *Phys. Rev. Lett.* **99**, 165505 (2007).
 - [4] S. Tatenko, K. Hirose, Y. Ohishi, and Y. Tatsumi, The Structure of Iron in Earth's Inner Core, *Science* **330**, 359 (2010).
 - [5] S. Anzellini, A. Dewaele, M. Mezouar, P. Loubeyre, and G. Morard, Melting of Iron at Earth's Inner Core Boundary Based on Fast X-ray Diffraction, *Science* **340**, 464 (2013).
 - [6] R. G. Kraus, R. J. Hemley, S. J. Ali, J. L. Belof, L. X. Benedict, J. Bernier, D. Braun, R. E. Cohen, G. W. Collins, F. Coppari, M. P. Desjarlais, D. Fratanduono, S. Hamel, A. Krygier, A. Lazicki, J. Mcnane, M. Millot, P. C. Myint, M. G. Newman, J. R. Rygg, D. M. Sterbentz, S. T. Stewart, L. Stixrude, D. C. Swift, C. Wehrenberg, and J. H. Eggert, Measuring the melting curve of iron at super-Earth core conditions, *Science* **375**, 202 (2022).
 - [7] L. Vočadlo, D. Alfè, M. J. Gillan, I. G. Wood, J. P. Brodholt, and G. D. Price, Possible thermal and chemical stabilization of body-centred-cubic iron in the Earth's core, *Nature* **424**, 536 (2003).
 - [8] A. B. Belonoshko, R. Ahuja, and B. Johansson, Stability of the body-centred-cubic phase of iron in the Earth's inner core, *Nature* **424**, 1032 (2003).
 - [9] W. Luo, B. Johansson, O. Eriksson, S. Arapan, P. Souvatzis, M. I. Katsnelson, and R. Ahuja, Dynamical stability of body center cubic iron at the Earth's core conditions, *Proceedings of the National Academy of Sciences* **107**, 9962 (2010).
 - [10] B. K. Godwal, F. González-Cataldo, A. K. Verma, L. Stixrude, and R. Jeanloz, Stability of iron crystal structures at 0.3–1.5 TPa, *Earth and Planetary Science Letters* **409**, 299 (2015).
 - [11] Y. Sun, F. Zhang, M. I. Mendelev, R. M. Wentzcovitch, and K.-M. Ho, Two-step nucleation of the Earth's inner core, *Proceedings of the National Academy of Sciences* **119**, e2113059119 (2022).
 - [12] Y. Sun, M. I. Mendelev, F. Zhang, X. Liu, B. Da, C.-Z. Wang, R. M. Wentzcovitch, and K.-M. Ho, Unveiling the effect of Ni on the formation and structure of Earth's inner core, *Proceedings of the National Academy of Sciences* **121**, e2316477121 (2024).
 - [13] G. Steinle-Neumann, L. Stixrude, R. E. Cohen, and O. Gülseren, Elasticity of iron at the temperature of the Earth's inner core, *Nature* **413**, 57 (2001).

- [14] L. Vočadlo, Ab initio calculations of the elasticity of iron and iron alloys at inner core conditions: Evidence for a partially molten inner core?, *Earth and Planetary Science Letters* **254**, 227 (2007).
- [15] A. B. Belonoshko, N. V. Skorodumova, S. Davis, A. N. Osipov, A. Rosengren, and B. Johansson, Origin of the Low Rigidity of the Earth's Inner Core, *Science* **316**, 1603 (2007).
- [16] H. Tkalcic and T.-S. Pham, Shear properties of Earth's inner core constrained by a detection of J waves in global correlation wavefield, *Science* **362**, 329 (2018).
- [17] A. B. Belonoshko, S. I. Simak, W. Olovsson, and O. Y. Vekilova, Elastic properties of body-centered cubic iron in Earth's inner core, *Phys. Rev. B* **105**, L180102 (2022).
- [18] D. Ikuta, E. Ohtani, H. Fukui, T. Sakai, D. Ishikawa, and A. Q. R. Baron, Sound velocity of hexagonal close-packed iron to the Earth's inner core pressure, *Nat Commun* **13**, 7211 (2022).
- [19] T. Costa de Lima, T.-S. Pham, X. Ma, and H. Tkalcic, An estimate of absolute shear-wave speed in the Earth's inner core, *Nat Commun* **14**, 4577 (2023).
- [20] X. Sha and R. E. Cohen, Elastic isotropy of ϵ -Fe under Earth's core conditions, *Geophysical Research Letters* **37**, 2009GL042224 (2010).
- [21] X. L. Sun and X. D. Song, The inner inner core of the earth: Texturing of iron crystals from three-dimensional seismic anisotropy, *Earth and Planetary Science Letters* **269**, 56 (2008), 312xi Times Cited:38 Cited References Count:62.
- [22] D. A. Frost and B. Romanowicz, On the orientation of the fast and slow directions of anisotropy in the deep inner core, *Physics of the Earth and Planetary Interiors* **286**, 101 (2019).
- [23] Z. Wu and W. Wang, Shear softening of earth's inner core as indicated by its high poisson ratio and elastic anisotropy, *Fundam Res* **5**, 264 (2025), wu, Zhongqing Wang, Wenzhong eng Netherlands 2022/08/24 Fundam Res. 2022 Aug 24;5(1):264-268. doi: 10.1016/j.fmre.2022.08.010. eCollection 2025 Jan.
- [24] J. E. Vidale, W. Wang, R. Wang, G. Pang, and K. Koper, Annual-scale variability in both the rotation rate and near surface of earth's inner core, *Nature Geoscience* **18**, 267 (2025).
- [25] J. Li and Y. Fei, 3.15 - Experimental Constraints on Core Composition, in *Treatise on Geochemistry (Second Edition)*, edited by H. D. Holland and K. K. Turekian (Elsevier, Oxford, 2014) pp. 527–557.
- [26] K. Hirose, B. Wood, and L. Vočadlo, Light elements in the Earth's core, *Nat Rev Earth Environ* **2**, 645 (2021).
- [27] L. Stixrude, E. Wasserman, and R. Cohen, Composition and temperature of earth's inner core, *Journal of Geophysical Research* **102**, 24729 (1997), tY - JOUR RP - IN FILE Y2 - ///.
- [28] D. Alfè, M. J. Gillan, and G. D. Price, Composition and temperature of the Earth's core constrained by combining ab initio calculations and seismic data, *Earth and Planetary Science Letters* **195**, 91 (2002).
- [29] R. A. Fischer, Y. Nakajima, A. J. Campbell, D. J. Frost, D. Harries, F. Langenhorst, N. Miyajima, K. Pollok, and D. C. Rubie, High pressure metal-silicate partitioning of ni, co, v, cr, si, and o, *Geochimica et Cosmochimica Acta* **167**, 177 (2015).
- [30] D. C. Rubie, S. A. Jacobson, A. Morbidelli, D. P. O'Brien, E. D. Young, J. de Vries, F. Nimmo, H. Palme, and D. J. Frost, Accretion and differentiation of the terrestrial planets with implications for the compositions of early-formed solar system bodies and accretion of water, *Icarus* **248**, 89 (2015).
- [31] R. B. Georg, A. N. Halliday, E. A. Schauble, and B. C. Reynolds, Silicon in the Earth's core, *Nature* **447**, 1102 (2007).
- [32] T. Liu and Z. Jing, Hydrogen and silicon are the preferred light elements in Earth's core, *Commun Earth Environ* **5**, 282 (2024).
- [33] L. Dubrovinsky, N. Dubrovinskaya, F. Langenhorst, D. Dobson, D. Rubie, C. Geßmann, I. A. Abrikosov, B. Johansson, V. I. Baykov, L. Vitos, T. L. Bihan, W. A. Crichton, V. Dmitriev, and H.-P. Weber, Iron-silica interaction at extreme conditions and the electrically conducting layer at the base of Earth's mantle, *Nature* **422**, 58 (2003).
- [34] J.-F. Lin, H. P. Scott, R. A. Fischer, Y.-Y. Chang, I. Kantor, and V. B. Prakapenka, Phase relations of Fe-Si alloy in Earth's core, *Geophysical Research Letters* **36**, 10.1029/2008GL036990 (2009).
- [35] R. A. Fischer, A. J. Campbell, D. M. Reaman, N. A. Miller, D. L. Heinz, P. Dera, and V. B. Prakapenka, Phase relations in the Fe-FeSi system at high pressures and temperatures, *Earth and Planetary Science Letters* **373**, 54 (2013).
- [36] S. Tatenio, Y. Kuwayama, K. Hirose, and Y. Ohishi, The structure of Fe-Si alloy in Earth's inner core, *Earth and Planetary Science Letters* **418**, 11 (2015).
- [37] D. Ikuta, E. Ohtani, and N. Hirao, Two-phase mixture of iron-nickel-silicon alloys in the Earth's inner core, *Commun Earth Environ* **2**, 1 (2021).
- [38] E. Edmund, G. Morard, M. A. Baron, A. Rivoldini, S. Yokoo, S. Boccato, K. Hirose, A. Pakhomova, and D. Antonangeli, The Fe-FeSi phase diagram at Mercury's core conditions, *Nat Commun* **13**, 387 (2022).
- [39] S. Yokoo, E. Edmund, G. Morard, M. A. Baron, S. Boccato, F. Decremps, K. Hirose, A. Pakhomova, and D. Antonangeli, Composition-dependent thermal equation of state of B2 Fe-Si alloys at high pressure, *American Mineralogist* **108**, 536 (2023).
- [40] Y. Nagaya, H. Gomi, K. Ohta, and K. Hirose, Equations of state for B2 and bcc Fe1-xSix, *Physics of the Earth and Planetary Interiors* **341**, 107046 (2023).
- [41] S. Fu, S. Chariton, V. B. Prakapenka, and S.-H. Shim, Core origin of seismic velocity anomalies at Earth's core-mantle boundary, *Nature* **615**, 646 (2023).
- [42] A. S. Côté, L. Vočadlo, D. P. Dobson, D. Alfè, and J. P. Brodholt, Ab initio lattice dynamics calculations on the combined effect of temperature and silicon on the stability of different iron phases in the Earth's inner core, *Physics of the Earth and Planetary Interiors 2008 IUGG SEDI Symposium*, **178**, 2 (2010).
- [43] H. Cui, Z. Zhang, and Y. Zhang, The effect of Si and S on the stability of bcc iron with respect to tetragonal strain at the Earth's inner core conditions, *Geophysical Research Letters* **40**, 2958 (2013).
- [44] Z. Li and S. Scandolo, Competing Phases of Iron at Earth's Core Conditions From Deep-Learning-Aided ab-initio Simulations, *Geophysical Research Letters* **51**, e2024GL110357 (2024).
- [45] Z. Li and S. Scandolo, Short-range order stabilizes a cubic iron alloy in Earth's inner core, *Nat Commun* **16**, 7574 (2025).

- [46] N. S. Golosov and A. M. Tolstik, Theory of order-disorder and order-order transformations in binary alloys with b.c.c. lattice—i, *Journal of Physics and Chemistry of Solids* **36**, 899 (1975).
- [47] T. Holland and R. Powell, Thermodynamics of order-disorder in minerals; ii, symmetric formalism applied to solid solutions, *American Mineralogist* **81**, 1425 (1996).
- [48] C. Jiang, C. Wolverton, J. Sofo, L.-Q. Chen, and Z.-K. Liu, First-principles study of binary bcc alloys using special quasirandom structures, *Physical Review B* **69**, 10.1103/PhysRevB.69.214202 (2004).
- [49] N. Kiyokane, Y. Chen, T. Yamashita, M. Nagoshi, T. Iguchi, and T. Mohri, B2-disorder phase boundary calculations in fe rich region of fe-si binary system with tetrahedron approximation of cvm, *Calphad* **56**, 207 (2017).
- [50] R. Dutta, S. J. Tracy, R. E. Cohen, F. Miozzi, K. Luo, J. Yang, P. C. Burnley, D. Smith, Y. Meng, S. Chariton, V. B. Prakapenka, and T. S. Duffy, Ultrahigh-pressure disordered eight-coordinated phase of Mg₂GeO₄: Analogue for super-Earth mantles, *Proceedings of the National Academy of Sciences* **119**, e2114424119 (2022).
- [51] R. Dutta, S. J. Tracy, and R. E. Cohen, High-pressure order-disorder transition in Mg₂SiO₄: Implications for super-earth mineralogy, *Phys. Rev. B* **107**, 184112 (2023).
- [52] D. Zheng, Y. Li, Y. Peng, R. Gong, Z.-K. Liu, and J. Deng, Cation disorder of mg₂si₄ in super-earth mantles, preprint 10.22541/essoar.173809982.21071819/v1 (2025).
- [53] S. Wei, L. G. Ferreira, J. E. Bernard, and A. Zunger, Electronic properties of random alloys: Special quasirandom structures, *Phys Rev B Condens Matter* **42**, 9622 (1990), we, S Ferreira, LG Bernard, JE Zunger, A eng 1990/11/15 Phys Rev B Condens Matter. 1990 Nov 15;42(15):9622-9649. doi: 10.1103/physrevb.42.9622.
- [54] A. van de Walle, P. Tiwary, M. de Jong, D. L. Olmsted, M. Asta, A. Dick, D. Shin, Y. Wang, L. Q. Chen, and Z. K. Liu, Efficient stochastic generation of special quasirandom structures, *Calphad* **42**, 13 (2013).
- [55] D. Alfè, M. J. Gillan, and G. D. Price, Constraints on the composition of the Earth's core from ab initio calculations, *Nature* **405**, 172 (2000).
- [56] A. B. Belonoshko, T. Lukinov, J. Fu, J. Zhao, S. Davis, and S. I. Simak, Stabilization of body-centred cubic iron under inner-core conditions, *Nature Geosci* **10**, 312 (2017).
- [57] A. B. Belonoshko, A. Rosengren, L. Burakovsky, D. L. Preston, and B. Johansson, Melting of fe and fe_{0.9375}si_{0.0625} at earth's core pressures studied using ab initio molecular dynamics, *Phys. Rev. B* **79**, 220102 (2009).
- [58] Y. Zhang, K. Luo, M. Hou, P. Driscoll, N. P. Salke, J. Minár, V. B. Prakapenka, E. Greenberg, R. J. Hemley, R. E. Cohen, and J.-F. Lin, Thermal conductivity of Fe-Si alloys and thermal stratification in Earth's core, *Proceedings of the National Academy of Sciences* **119**, e2119001119 (2022).
- [59] C. Liu and R. E. Cohen, Electrical resistivity, thermal conductivity, and viscosity of Fe-H alloys at Earth's core conditions, *Phys. Rev. B* **111**, 094101 (2025).
- [60] A. M. Dziewonski and D. L. Anderson, Preliminary reference Earth model, *Physics of the Earth and Planetary Interiors* **25**, 297 (1981).
- [61] T. Wang and X. Song, Support for equatorial anisotropy of Earth's inner-inner core from seismic interferometry at low latitudes, *Physics of the Earth and Planetary Interiors Special Issue:15th SEDI Conference*, **276**, 247 (2018).
- [62] D. A. Frost and B. Romanowicz, On the orientation of the fast and slow directions of anisotropy in the deep inner core, *Physics of the Earth and Planetary Interiors* **286**, 101 (2019).
- [63] S. Wang and H. Tkalčić, Shear-Wave Anisotropy in the Earth's Inner Core, *Geophysical Research Letters* **48**, e2021GL094784 (2021).
- [64] H. Tkalčić, S. Wang, and T.-S. Phạm, Shear Properties of Earth's Inner Core, *Annual Review of Earth and Planetary Sciences* **50**, 153 (2022).
- [65] X. Deng, C. Luo, R. M. Wentzcovitch, G. A. Abers, and Z. Wu, Elastic Anisotropy of Lizardite at Subduction Zone Conditions, *Geophysical Research Letters* **49**, e2022GL099712 (2022).
- [66] E. Kolesnikov, I. Kuppenko, M. Achorn, C. Plückerthun, H.-P. Liermann, S. Merkel, and C. Sanchez-Valle, Strength and seismic anisotropy of textured FeSi at planetary core conditions, *Front. Earth Sci.* **10**, 10.3389/feart.2022.974148 (2022).
- [67] Z. Wu and W. Wang, Shear softening of earth's inner core as indicated by its high poisson ratio and elastic anisotropy, *Fundamental Research* **5**, 264 (2025).
- [68] Y. Li, L. Vočadlo, and J. P. Brodholt, The elastic properties of *hcp*-Fe alloys under the conditions of the Earth's inner core, *Earth and Planetary Science Letters* **493**, 118 (2018).
- [69] Y. He, S. Sun, D. Y. Kim, B. G. Jang, H. Li, and H.-k. Mao, Superionic iron alloys and their seismic velocities in Earth's inner core, *Nature* **602**, 258 (2022).
- [70] A. J. Wilson, C. J. Davies, A. M. Walker, M. Pozzo, D. Alfè, and A. Deuss, The formation and evolution of the Earth's inner core, *Nat Rev Earth Environ* **6**, 140 (2025).
- [71] T. Wang, X. Song, and H. H. Xia, Equatorial anisotropy in the inner part of Earth's inner core from autocorrelation of earthquake coda, *Nature Geosci* **8**, 224 (2015).
- [72] A. van de Walle, M. Asta, and G. Ceder, The alloy theoretic automated toolkit: A user guide, *Calphad* **26**, 539 (2002).
- [73] G. Kresse and J. Furthmüller, Efficient iterative schemes for ab initio total-energy calculations using a plane-wave basis set, *Phys. Rev. B* **54**, 11169 (1996).
- [74] P. E. Blöchl, Projector augmented-wave method, *Phys. Rev. B* **50**, 17953 (1994).
- [75] J. P. Perdew, K. Burke, and M. Ernzerhof, Generalized Gradient Approximation Made Simple, *Phys. Rev. Lett.* **77**, 3865 (1996).
- [76] M. P. Allen and D. J. Tildesley, *Computer Simulation of Liquids* (Oxford University Press, 2017).
- [77] H. Ebert, D. Ködderitzsch, and J. Minár, Calculating condensed matter properties using the KKR-Green's function method—recent developments and applications, *Rep. Prog. Phys.* **74**, 096501 (2011).
- [78] J. Minár, Correlation effects in transition metals and their alloys studied using the fully self-consistent KKR-based LSDA + DMFT scheme, *J. Phys.: Condens. Matter* **23**, 253201 (2011).
- [79] V. Wang, N. Xu, J.-C. Liu, G. Tang, and W.-T. Geng, Vaspkit: A user-friendly interface facilitating high-throughput computing and analysis using vasp code,

ACKNOWLEDGMENTS

We thank Russell J. Hemley for insightful discussions and valuable suggestions that greatly improved this work. This work is supported by the US National Science Foundation CSEDI grant EAR-1901813 and the Carnegie Institution for Science. We gratefully acknowledge supercomputer support from the Resnick High Performance Computing Center. The authors gratefully acknowledge the Gauss Centre for Supercomputing e.V. (www.gauss-centre.eu) for funding this project by providing computing time on the GCS Supercomputer SuperMUC-NG at Leibniz Supercomputing Centre

ADDITIONAL INFORMATION

Supplemental Information is available in the online version of the paper.

COMPETING FINANCIAL INTERESTS

The authors declare no competing financial interests.

Supplemental Materials

Order–Disorder in Fe–Si Alloys: Implications for Seismic Anisotropy and Thermal Evolution of Earth’s Inner Core

Cong Liu^{1,*}, Xin Deng¹, and R. E. Cohen^{1,†}

¹Extreme Materials Initiative, Earth and Planets Laboratory, Carnegie Institution for Science,
5241 Broad Branch Road NW, Washington, DC 20015, USA

*Corresponding author: cliu10@carnegiescience.edu

†rcohen@carnegiescience.edu

1. Fig. S1 illustrates the two-site model in the B2, hcp, and fcc phases.
2. Fig. S2 shows the enthalpy as a function of the order parameter Q at 330 GPa.
3. Fig. S3 presents the powder diffraction patterns of the bcc and B2 phases of the Fe–Si alloy.
4. Fig. S4 shows the Gibbs free energy ΔG of the Fe–Si alloy.
5. Fig. S5 illustrates the evolution of the configurational entropy in the two-site model.
6. Fig. S6 shows the evolution of vibrational entropy with composition at 6000 K from molecular dynamics simulations.
7. Fig. S8 shows the chemical potential $\Delta\mu$ of the Fe–Si alloy.
8. Fig. S7 illustrates the thermodynamic competition between the B2 and bcc phases across varying temperatures and compositions. conditions, indicating solid-like atomic behavior.
9. Fig. S9 presents the compressional wave velocity (V_P) and shear wave velocity (V_S) as functions of propagation direction relative to the c -axis.
10. Fig. S10 shows the pressure dependence of seismic velocities.
11. Fig. S11 shows the density- and composition-dependent Poisson’s ratio.
12. Fig. S12 shows the effect of supercell size on the SQS simulations.
13. Fig. S13 shows the vibrational density of states and mean-square displacement of $\text{Fe}_{0.875}\text{Si}_{0.125}$ alloy under Earth’s inner-core
14. Table S1 lists the Fe and Si concentrations at each site in the two-site model.
15. Table S2 lists the elastic constants of the disordered-phase $\text{Fe}_{0.875}\text{Si}_{0.125}$ alloy under Earth’s inner-core conditions.

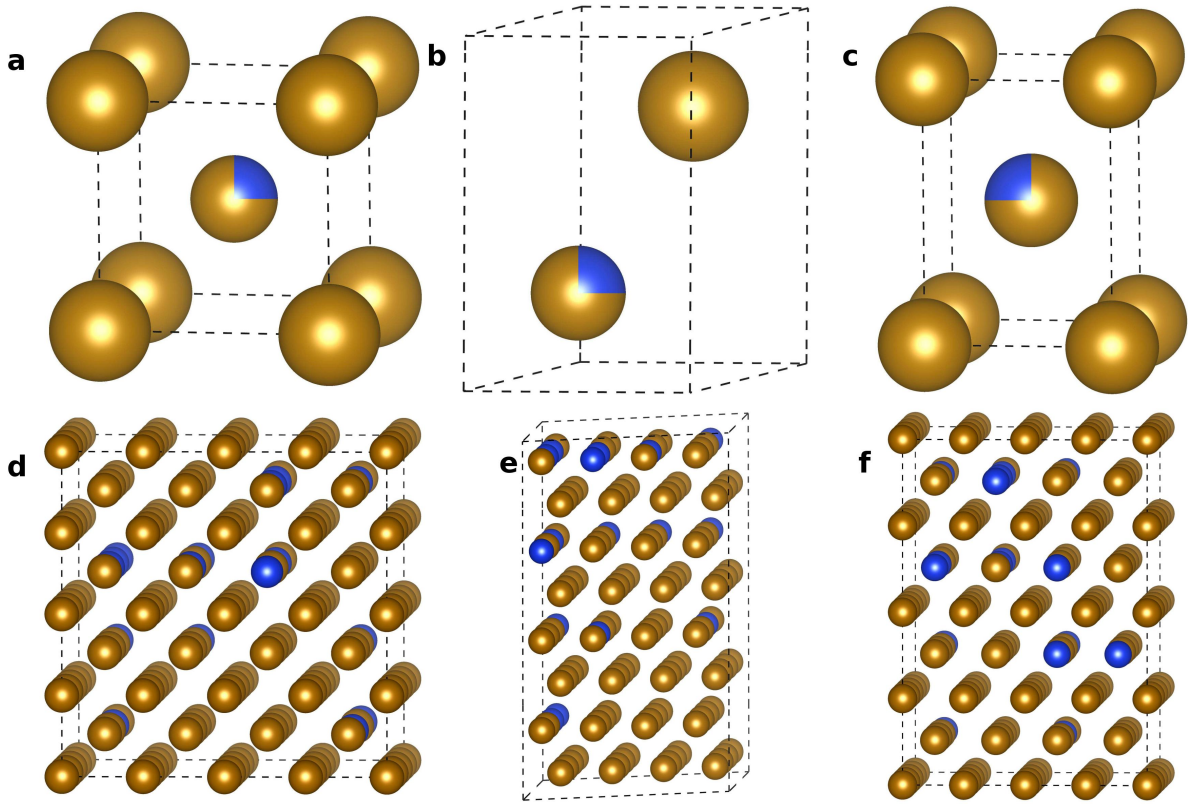


Fig. S1. **Two-site model and corresponding SQS** for (a, d) B2, (b, e) hcp, and (c, f) fcc phases. The two-site model of the fcc phase is transformed from the four-atom conventional fcc cell. Iron and silicon atoms are shown in brown and blue, respectively. The figure shows fully ordered phases ($Q = 1$) at a composition of $\text{Fe}_{0.875}\text{Si}_{0.125}$, where Si atoms partially substitute on a specific crystallographic site.

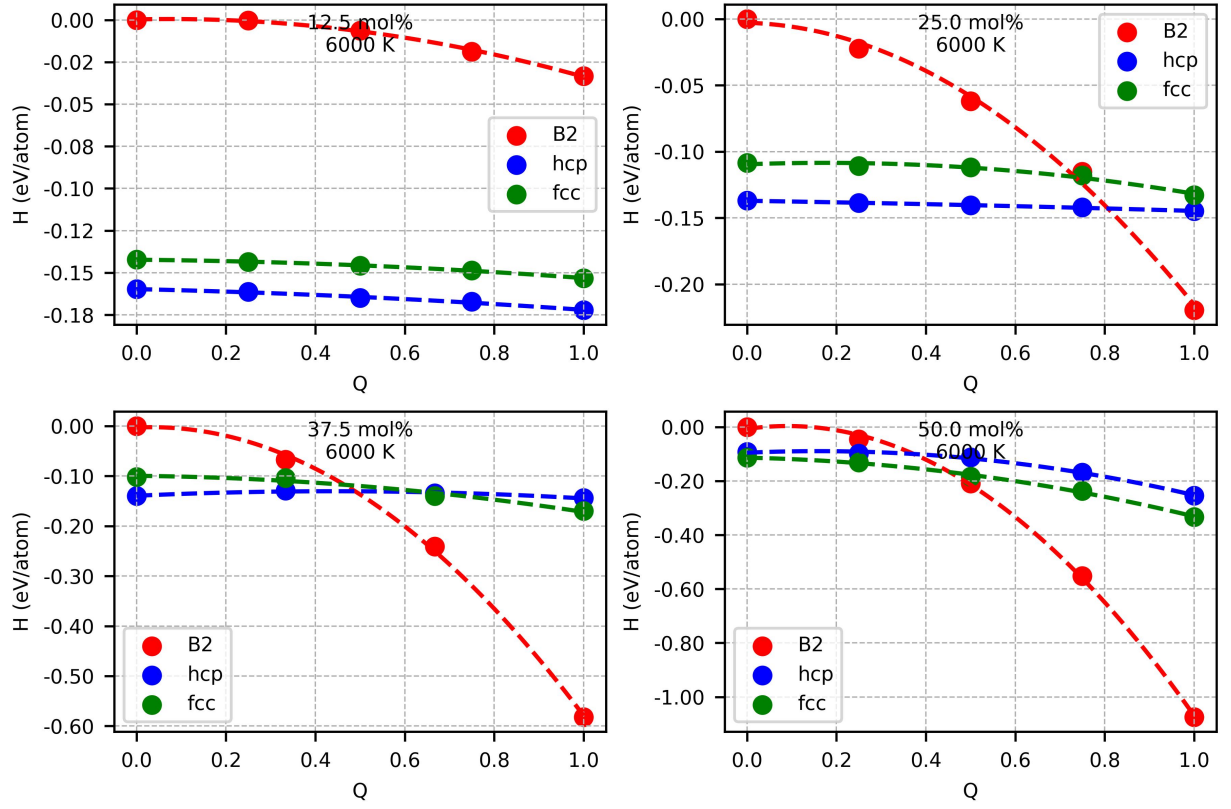


Fig. S2. **Enthalpy of Fe–Si alloys at 330 GPa and 6000 K.** High-temperature enthalpies were obtained from molecular dynamics simulations, averaged over the final 5 ps of equilibrated trajectories. The order parameter Q was varied for B2 (red), hcp (blue), and fcc (green) phases of Fe–Si alloys with Si content of 12.5, 25.0, 37.5, and 50.0 mol%. Enthalpies of the B2 phase at $Q = 0$ are shifted to zero for comparison.

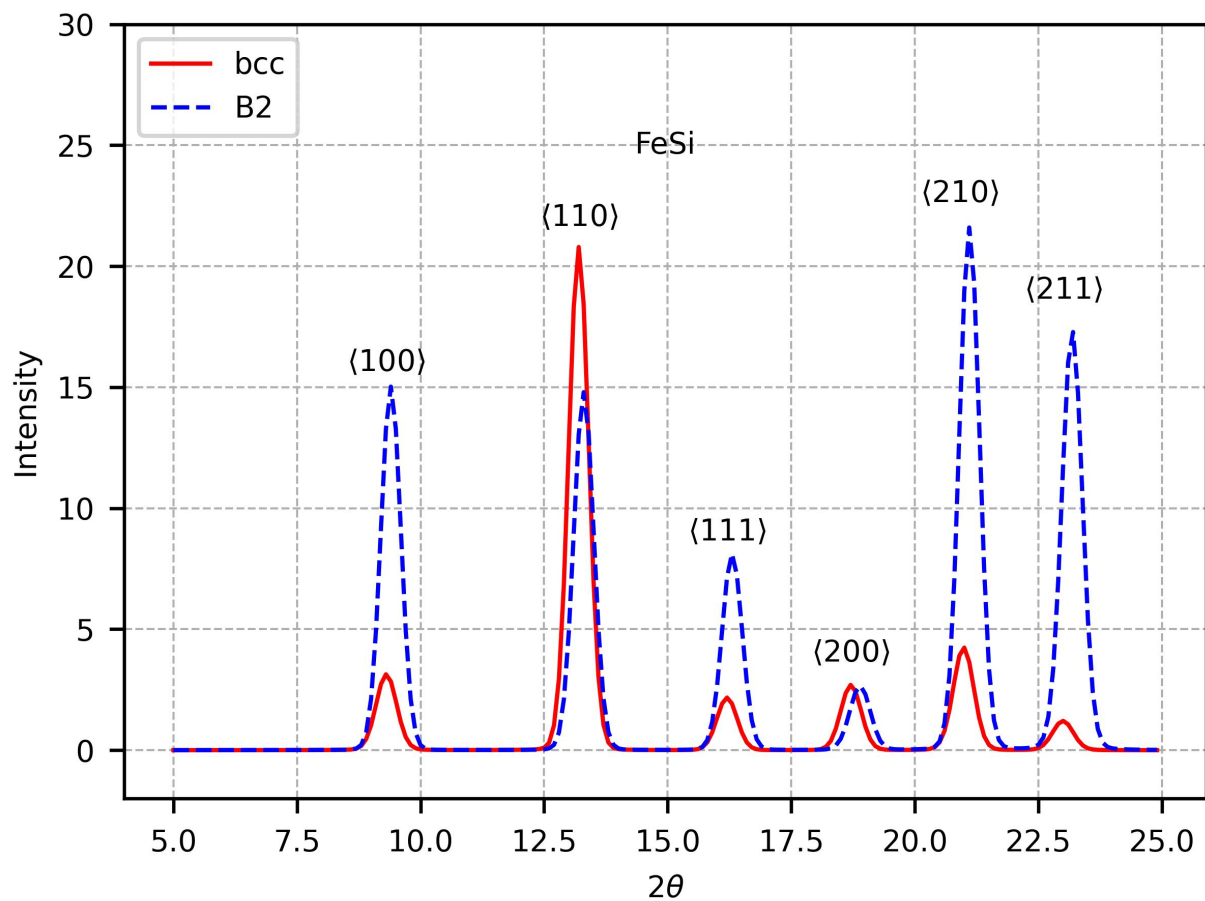


Fig. S3. Powder diffraction patterns of bcc/B2 phase $\text{Fe}_{0.875}\text{Si}_{0.125}$ alloys at Earth's inner-core conditions. X-ray diffraction data were derived from molecular dynamics snapshots of disordered (solid red) and ordered (dashed blue) structures.

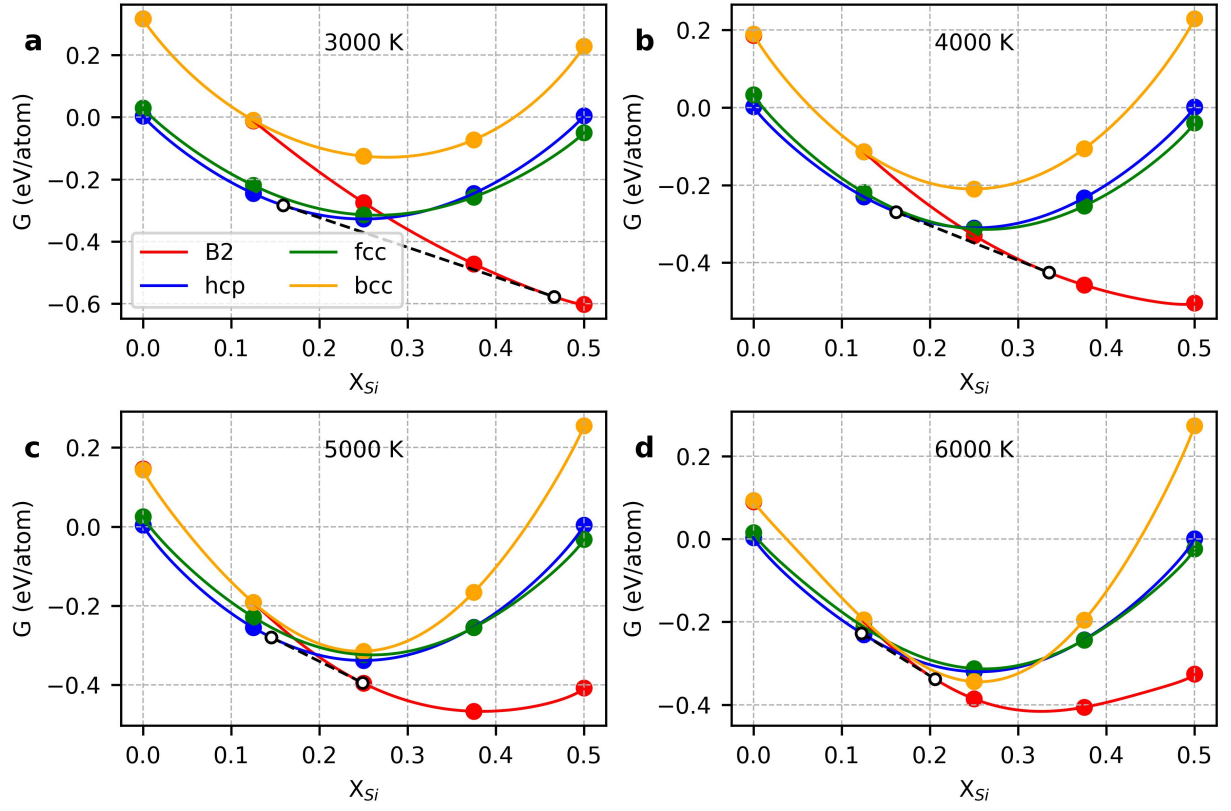


Fig. S4. **Gibbs free energy G of Fe-Si alloys.** Results for B2 (red), hcp (blue), fcc (green), and bcc (orange) phases with different compositions at (a) 3000 K, (b) 4000 K, (c) 5000 K, and (d) 6000 K. All Gibbs free energy curves were rescaled by removing the linear part from the hcp phase such that $\Delta G = 0$ at both ends. The dashed lines indicate the common tangent between B2 and hcp phases.

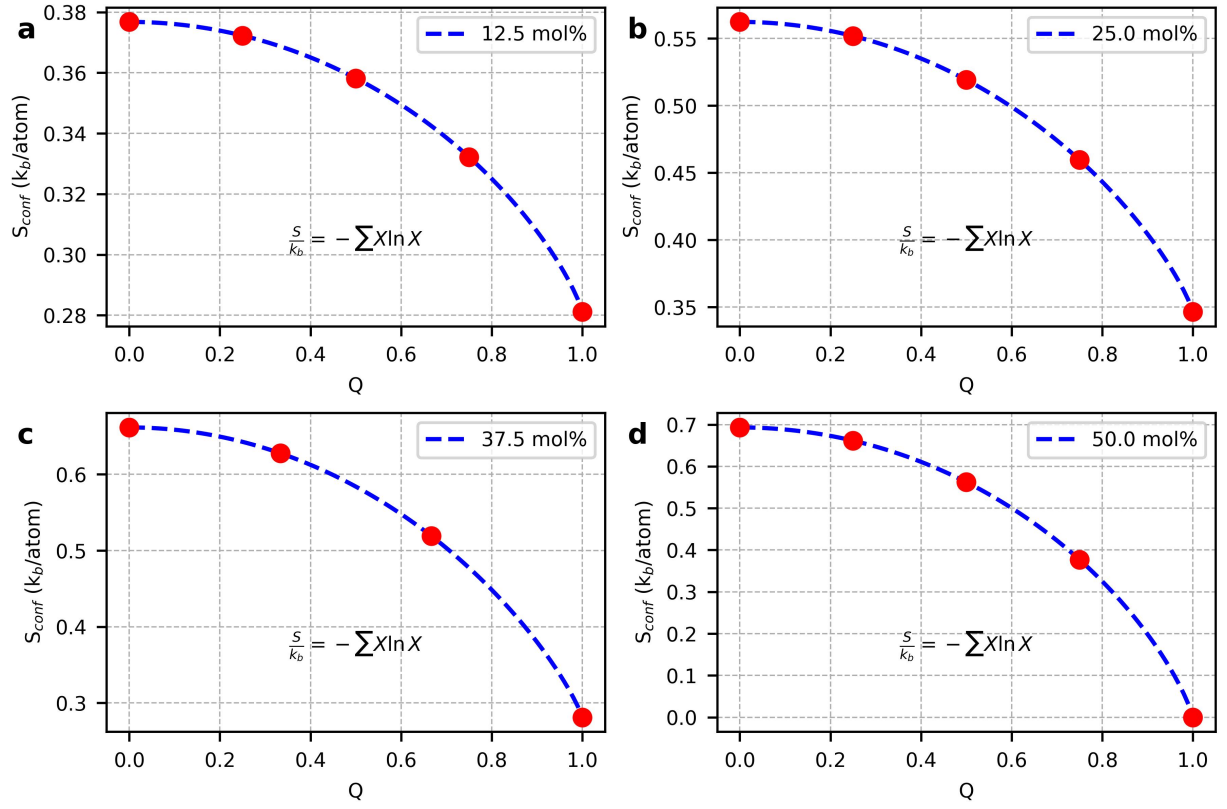


Fig. S5. **Evolution of configurational entropy in the two-site model.** The entropy varies with the order parameter Q for Si concentrations of 12.5, 25.0, 37.5, and 50.0 mol%. X denotes the occupation of Fe and Si atoms at each site.

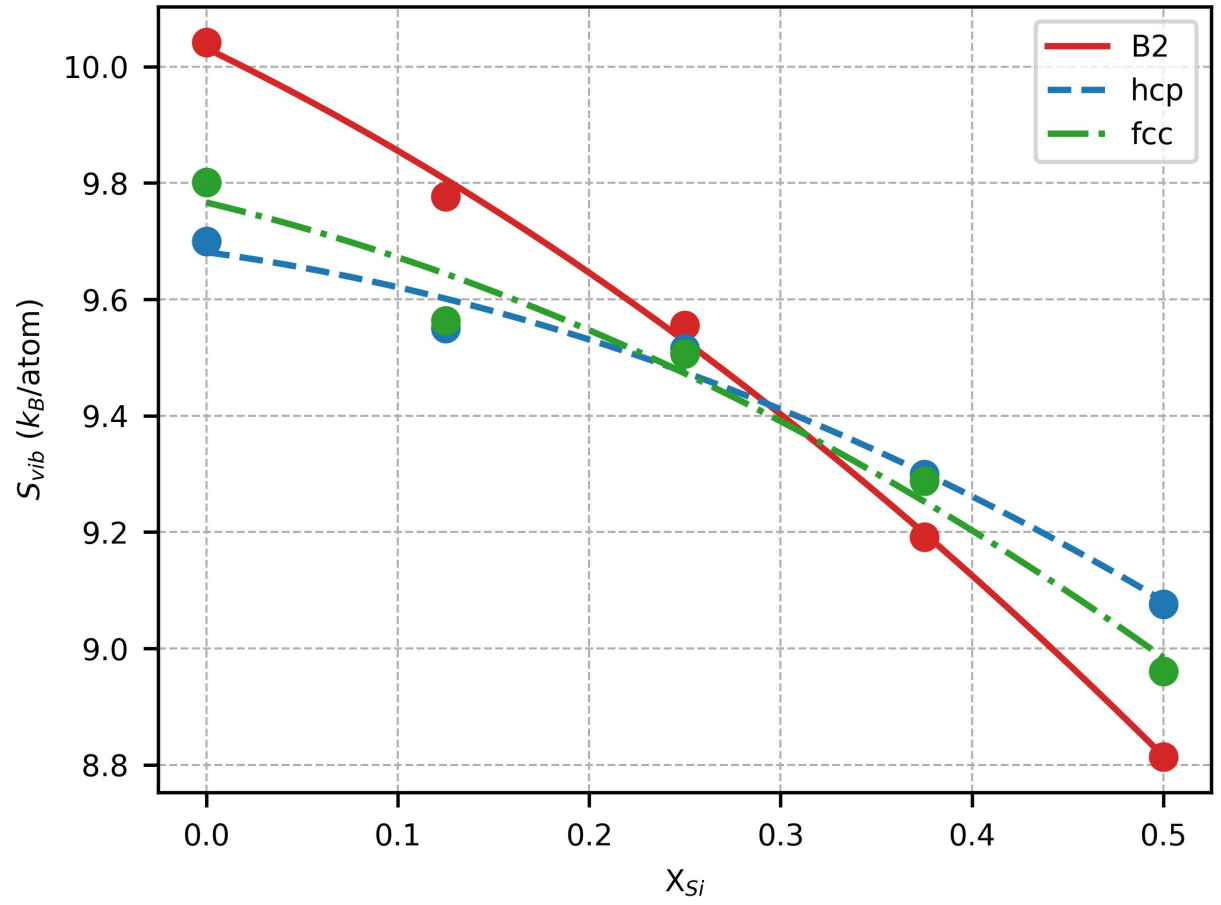


Fig. S6. **Evolution of vibrational entropy with Si content.** Results obtained from molecular dynamics simulations at 330 GPa and 6000 K. The vibrational entropy exhibits minor variation among different order parameters (Q) for Si contents below 12.5 mol%.

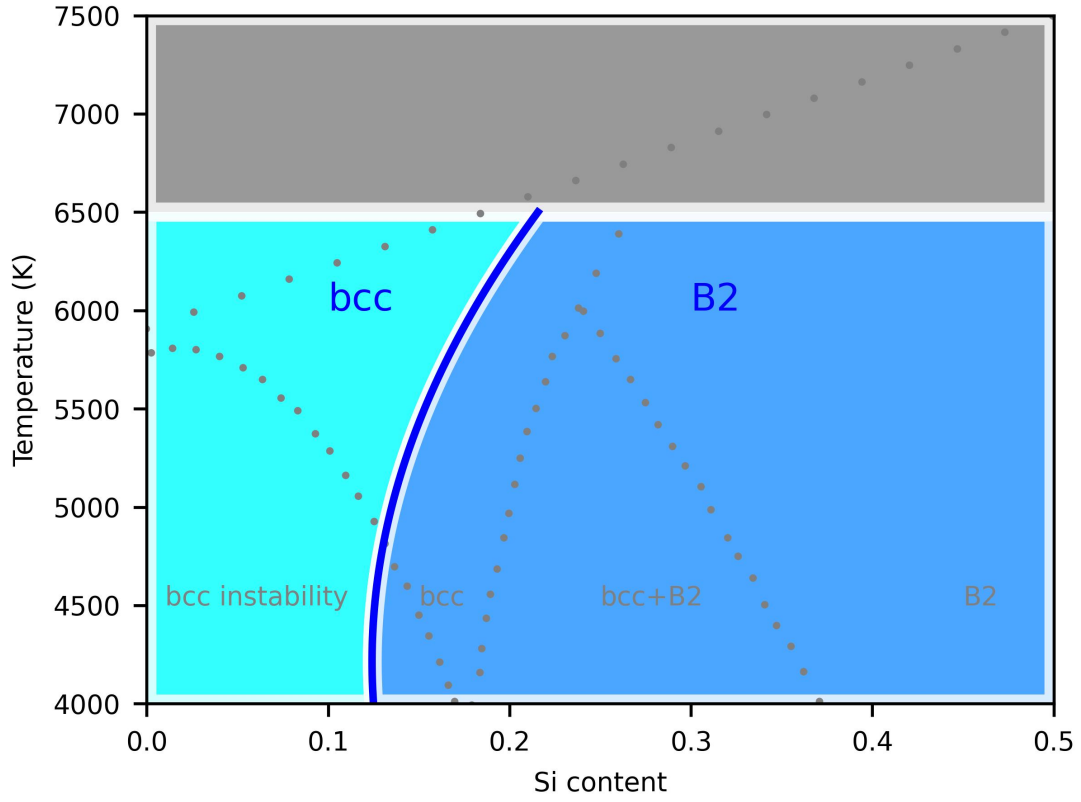


Fig. S7. **Schematic diagram of the Fe–Si system** restricted to the bcc and B2 phases. The solid blue line represents the phase boundary between bcc (cyan) and B2 (blue), showing that the bcc phase is stabilized at higher temperatures and lower Si concentrations. For comparison, the phase boundary from Ref. [45] is shown as dashed gray lines, indicating a coexistence region between the bcc and B2 phases. The shaded grey regions above 6300 K indicate the constraints imposed by melting curves beyond the range of our simulations.

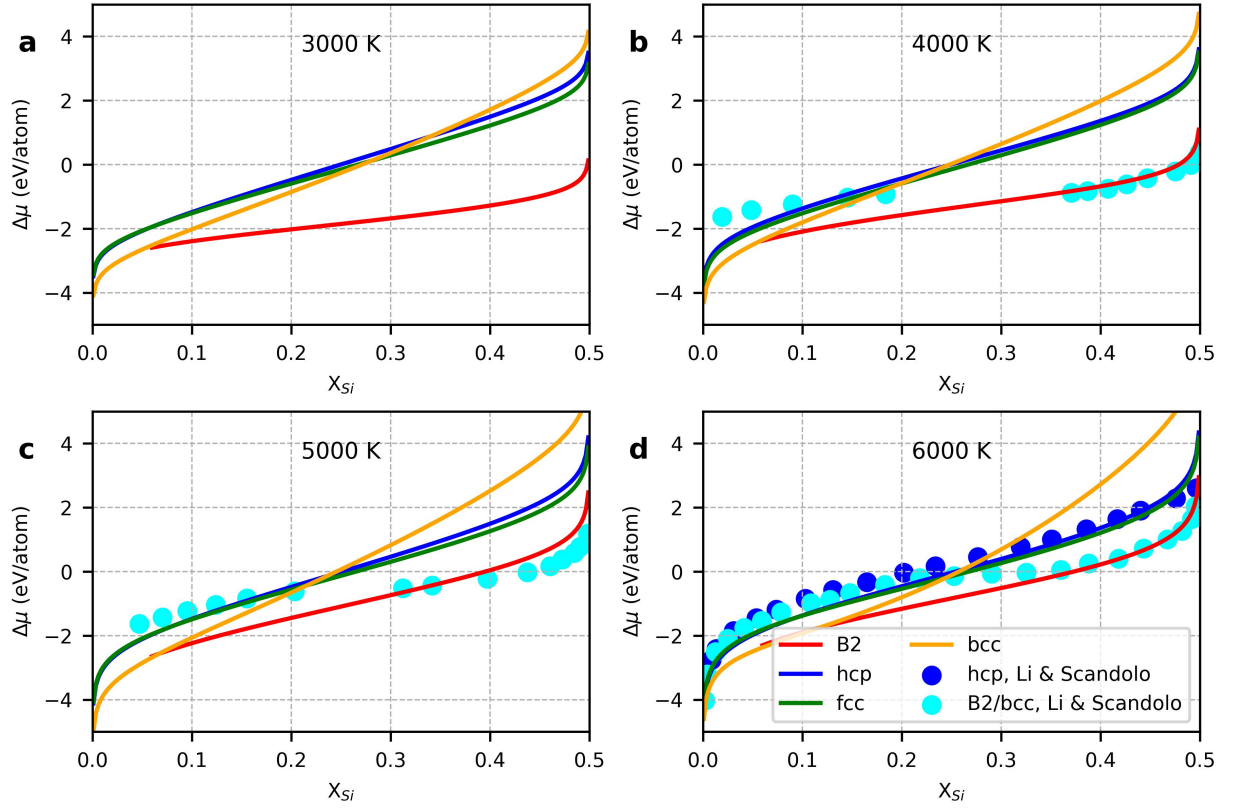


Fig. S8. **Chemical potential difference** ($\Delta\mu$) between Si and Fe as a function of Si concentration, derived from the Gibbs free energy curves of the B2 (red), hcp (blue), fcc (green), and bcc (orange) phases at (a) 3000 K, (b) 4000 K, (c) 5000 K, and (d) 6000 K. For comparison, chemical potentials from Li and Scandolo [45] are shown as reference points for the hcp phase (blue symbols) and the B2/bcc phases (cyan symbols).

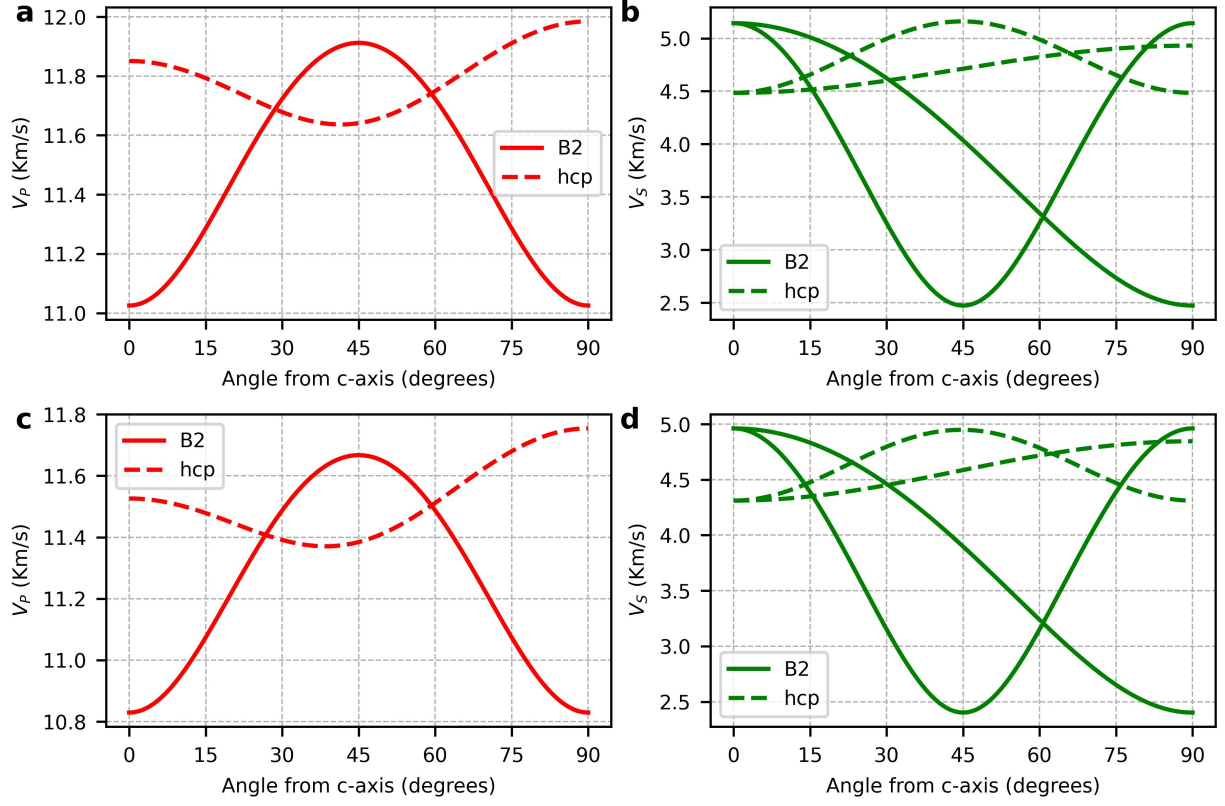


Fig. S9. **Directional dependence of seismic wave velocities.** Compressional (V_P) and shear (V_S) wave velocities of B2 and hcp $\text{Fe}_{0.875}\text{Si}_{0.125}$ alloys as functions of propagation direction relative to the c -axis at 5000 K (a, b) and 6000 K (c, d). In the B2 structure, $\text{Fe}_{0.875}\text{Si}_{0.125}$ stabilizes in the disordered ($Q = 0$, bcc) phase.

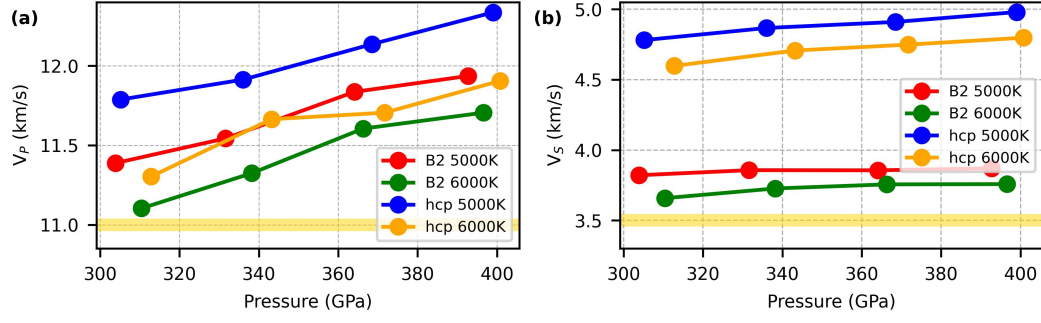


Fig. S10. **Seismic velocities of Fe–Si alloys as a function of pressure.** Calculated (a) compressional-wave (V_P) and (b) shear-wave (V_S) velocities of Fe_{0.875}Si_{0.125} alloys in the B2 and hcp phases at 5000 K and 6000 K over the pressure range 300–400 GPa. The yellow band indicates the average seismic velocities of the Earth's inner core [60]. In the B2 structure, Fe_{0.875}Si_{0.125} stabilizes in a disordered configuration ($Q = 0$, corresponding to the bcc phase). Both V_P and V_S increase with pressure and decrease with temperature, reflecting compression stiffening and thermal softening, respectively. Compared to the B2 phase, the hcp phase exhibits higher seismic velocities across all conditions, exceeding the seismological reference values. In contrast, the B2 phase shows a closer match to the observed inner-core shear-wave velocity, particularly in V_S .

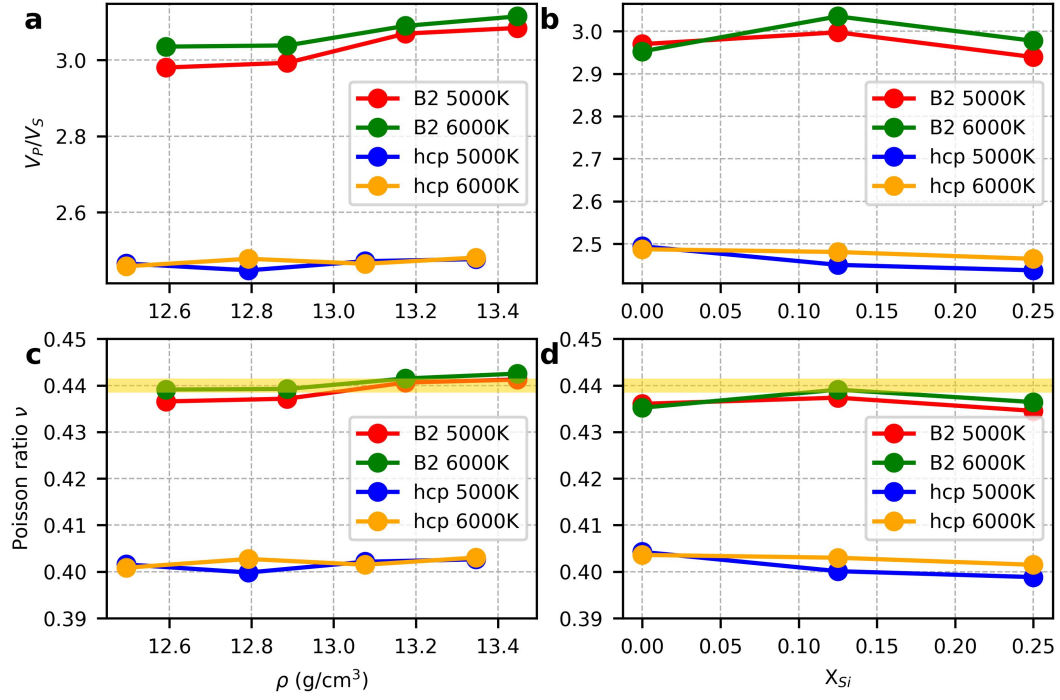


Fig. S11. **Variation of V_P/V_S and Poisson's ratio ν** of Fe-Si alloys with (a, c) density and (b, d) composition in B2 and hcp phases at 5000 K and 6000 K. The yellow region marks the observed Poisson's ratio of ~ 0.44 [60]. In the B2 structure, $\text{Fe}_{0.875}\text{Si}_{0.125}$ stabilizes in the disordered ($Q = 0$, bcc) phase, while $\text{Fe}_{0.75}\text{Si}_{0.25}$ remains ordered ($Q = 1$) at 5000–6000 K. The B2 phase exhibits a significantly higher V_P/V_S ratio than the hcp phase, yielding a Poisson's ratio that closely matches the seismological observation of 0.44.

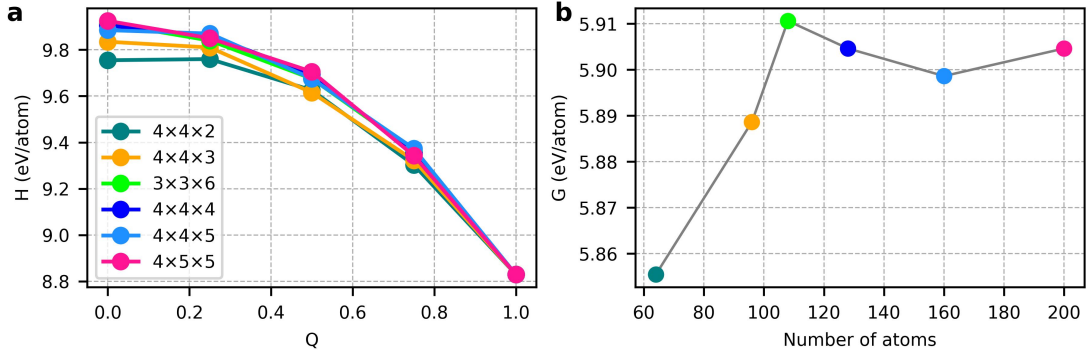


Fig. S12. **Effect of supercell size on SQS simulations.** (a) Enthalpy of B2 $\text{Fe}_{0.5}\text{Si}_{0.5}$ at 330 GPa as a function of Q , computed using different supercell sizes. (b) Gibbs free energy of disordered B2 phase (bcc, $Q = 0$) Fe-Si at 6000 K versus supercell atom number.

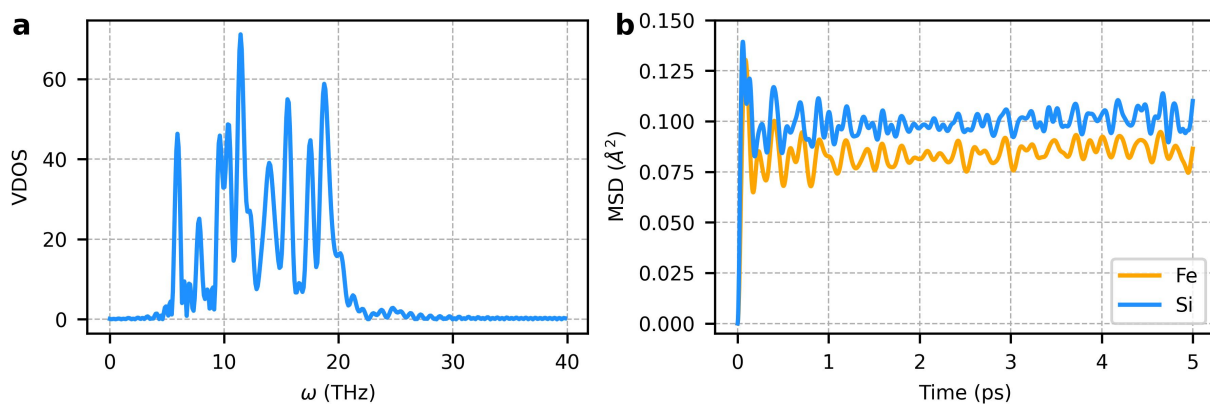


Fig. S13. **Vibrational properties of $\text{Fe}_{0.875}\text{Si}_{0.125}$ alloy at Earth's inner-core conditions.** (a) Vibrational density of states (VDOS) and (b) mean-square displacement obtained from first-principles molecular dynamics (FPMD) simulations indicate solid-like atomic behavior without diffusivity.

Table. S1. Composition, order parameter Q , and Fe/Si concentrations at each site in the two-site model.

Composition	Q	Site 1		Site 2	
		Fe ₁	Si ₁	Fe ₂	Si ₂
Fe _{1.000} Si _{0.000}	1.000	1.00000	0.00000	1.00000	0.00000
	0.000	0.87500	0.12500	0.87500	0.12500
	0.250	0.90625	0.09375	0.84375	0.15625
	0.500	0.93750	0.06250	0.81250	0.18750
Fe _{0.875} Si _{0.125}	0.750	0.96875	0.03125	0.78125	0.21875
	1.000	1.00000	0.00000	0.75000	0.25000
	0.000	0.75000	0.25000	0.75000	0.25000
	0.250	0.81250	0.18750	0.68750	0.31250
Fe _{0.750} Si _{0.250}	0.500	0.87500	0.12500	0.62500	0.37500
	0.750	0.93750	0.06250	0.56250	0.43750
	1.000	1.00000	0.00000	0.50000	0.50000
	0.000	0.62500	0.37500	0.62500	0.37500
Fe _{0.625} Si _{0.375}	0.333	0.75000	0.25000	0.50000	0.50000
	0.667	0.87500	0.12500	0.37500	0.62500
	1.000	1.00000	0.00000	0.25000	0.75000
	0.000	0.50000	0.50000	0.50000	0.50000
Fe _{0.500} Si _{0.500}	0.250	0.62500	0.37500	0.37500	0.62500
	0.500	0.75000	0.25000	0.25000	0.75000
	0.750	0.87500	0.12500	0.12500	0.87500
	1.000	1.00000	0.00000	0.00000	1.00000

Table. S2. Densities (ρ), temperature (T), pressure (P), elastic constants (C_{ij}), bulk modulus (B), Hill averaged shear modulus (G), seismic velocities (V_P , V_S) and Chung–Buessem anisotropy (A_{CB}) of pure Fe and disordered $\text{Fe}_{0.875}\text{Si}_{0.125}$ alloy in B2 and hcp phases at 5000 K, 6000 K, and 6500 K. In the B2 structure, $\text{Fe}_{0.875}\text{Si}_{0.125}$ stabilizes in the disordered ($Q = 0$, bcc-like) phase, while $\text{Fe}_{0.75}\text{Si}_{0.25}$ remains ordered ($Q = 1$) at 5000–6000 K.

phase	comp.	ρ (g/cm ³)	T (K)	P (GPa)	C_{11} (GPa)	C_{12} (GPa)	C_{44} (GPa)	C_{13} (GPa)	C_{33} (GPa)	B (GPa)	G (GPa)	V_P (km/s)	V_S (km/s)	A_{CB} (%)
bcc	pure Fe	13.55	5000	332.9	1497	1351	315	–	–	1400	183	10.75	3.62	23.4
bcc	pure Fe	13.55	6000	337.4	1455	1309	305	–	–	1391	180	10.60	3.59	18.7
hcp	pure Fe	13.72	5000	338.2	1808	1204	245	1102	1751	1354	277	11.05	4.43	0.4
hcp	pure Fe	13.72	6000	345.7	1733	1159	241	1063	1687	1303	266	10.82	4.35	0.3
B2	$\text{Fe}_{0.875}\text{Si}_{0.125}$	12.79	5000	331.6	1590	1430	346	–	–	1483	194	11.54	3.85	23.3
B2	$\text{Fe}_{0.875}\text{Si}_{0.125}$	12.79	6000	338.2	1534	1383	322	–	–	1433	182	11.32	3.73	22.9
B2	$\text{Fe}_{0.875}\text{Si}_{0.125}$	12.79	6500	344.7	1498	1349	312	–	–	1410	171	11.12	3.62	22.4
hcp	$\text{Fe}_{0.875}\text{Si}_{0.125}$	12.89	5000	336.0	1893	1252	265	1170	1851	1424	304	11.91	4.86	0.7
hcp	$\text{Fe}_{0.875}\text{Si}_{0.125}$	12.89	6000	343.2	1821	1202	245	1140	1751	1373	285	11.66	4.70	0.6
hcp	$\text{Fe}_{0.875}\text{Si}_{0.125}$	12.89	6500	347.2	1745	1210	242	1153	1680	1341	279	11.49	4.67	0.9
B2	$\text{Fe}_{0.75}\text{Si}_{0.25}$	11.96	5000	335.4	1710	1533	369	–	–	1405	212	12.08	4.11	22.8
B2	$\text{Fe}_{0.75}\text{Si}_{0.25}$	11.96	6000	342.7	1615	1450	344	–	–	1358	199	11.85	3.98	23.2
hcp	$\text{Fe}_{0.75}\text{Si}_{0.25}$	12.10	5000	338.8	2037	1372	298	1258	1998	1522	327	12.53	5.14	0.9
hcp	$\text{Fe}_{0.75}\text{Si}_{0.25}$	12.10	6000	345.7	1968	1318	283	1207	1915	1467	312	12.25	4.97	0.8